THESIS FOR THE DEGREE OF DOCTOR OF PHILOSOPHY

Kinetics and charge transfer in nanocatalysis

Rasmus Svensson

Department of Physics
CHALMERS UNIVERSITY OF TECHNOLOGY
Göteborg, Sweden 2026

Kinetics and charge transfer in nanocatalysis
Rasmus Svensson
ISBN 978-91-8103-383-0

Doktorsavhandlingar vid Chalmers tekniska högskola
Ny serie nr. 5840
ISSN 0346-718X
https://doi.org/10.63959/chalmers.dt/5840

Department of Physics
Chalmers University of Technology
SE-412 96 Göteborg, Sweden
Telephone +46 (0)31 772 10 00

Cover: Visualization of processes occurring at catalyst interfaces.

Chalmers digitaltryck
Göteborg, Sweden 2026

Kinetics and charge transfer in nanocatalysis

Rasmus Svensson
Department of Physics
Chalmers University of Technology

Abstract

Heterogeneous catalysis is crucial in a range of environmental and industrial technologies, ranging from emission control and the utilization of greenhouse gases to the production of fuels and chemicals. Understanding and optimizing the catalytic performance is challenging, as industrial catalysts are generally ill-defined mixtures of metal and oxide phases. Moreover, the structures and chemical properties respond sensitively to the reaction environments.

Atomic scale understanding of catalytic reactions under relevant reaction conditions is beneficial to aid the discovery of catalyst materials. In this thesis, quantum mechanical calculations are combined with kinetic simulations to elucidate the synergy between different catalyst constituents and the effects of reaction environment on catalytic reactions. To investigate the metal/metal interplay and the influence of an aqueous reaction environment, the direct formation of H_2O_2 from H_2 and O_2 over water-solvated PdAu single-atom alloy nanoparticles is explored. The interplay between metal and oxide phases is studied in connection with CO_2 hydrogenation to methanol. The dynamic behavior of nanoparticles is probed using kinetic Monte Carlo simulations in inert and reactive atmospheres.

The formation of H_2O_2 relies on the facile desorption of protons from the surface to the water solution, leaving the electrons in the metal surface. *Ab initio* molecular dynamics simulations reveal that the metal/water interface affects the adsorption properties of H_2 and O_2 also on other metal surfaces. Similar synergetic effects occur between metal nanoparticles and oxide supports, where the adsorption of H_2 on oxides is stabilized close to metal nanoparticles, owing to an oxide-to-metal charge transfer. The metal/oxide synergy results in novel catalytic properties under reaction conditions, which is found to have important implications for the reaction intermediates in the case of CO_2 hydrogenation to methanol over Cu/ZnO catalysts.

The work highlights the interplay between the different phases in nano-sized catalyst materials. The synergy results in modified catalyst properties and new catalytic pathways under reaction conditions. Understanding of these processes at the atomic scale could potentially be used to optimize new materials in heterogeneous catalysis.

Keywords: heterogeneous catalysis, density functional theory, kinetic Monte Carlo, metal/water interface, metal/oxide synergy, charge transfer, kinetics

LIST OF PUBLICATIONS

I **Site communication in direct formation of H_2O_2 over single-atom Pd@Au nanoparticles**
Rasmus Svensson and Henrik Grönbeck
J. Am. Chem. Soc., **145**, 11579–11588 (2023)

II **Spontaneous charge separation at the metal-water interface**
Rasmus Svensson and Henrik Grönbeck
ChemPhysChem, **25**, e202400099 (2024)

III **Dynamics of dilute nanoalloy catalysts**
Rasmus Svensson and Henrik Grönbeck
J. Phys. Chem. Lett., **15**, 7885-7891 (2024)

IV **Charge transfer across the metal/oxide interface determines the rate of CO_2 hydrogenation to methanol over Cu/ZnO catalysts**
Jonas A. Boysen, Rasmus Svensson, Niels. D. Nielsen, Mads Lützen, Lin Bigom-Eriksen, Andrey Shavorskiy, Thomas E. Andersen, Jacob L. Fischer, Jean-Claude Grivel, Christian D. Damsgaard, Anker D. Jensen, Henrik Grönbeck, and Jakob M. Christensen
Submitted

V **Modified sites by hydrogen adsorption in metal/oxide catalysts**
Rasmus Svensson and Henrik Grönbeck
Submitted

VI **Oxide to metal charge transfer facilitates oxygen vacancy formation in metal/oxide systems**
Rasmus Svensson and Henrik Grönbeck
In Manuscript

AUTHOR CONTRIBUTION

I I performed all calculations, implemented the kinetic Monte Carlo simulations and wrote the first draft of the paper. The paper was finalized together with my co-author.

II I performed all calculations and wrote the first draft of the paper. The paper was finalized together with my co-author.

III I performed all calculations, implemented the kinetic Monte Carlo simulations and wrote the first draft of the paper. The paper was finalized together with my co-author.

IV I performed all calculations and wrote the first draft of the corresponding parts of the manuscript. The manuscript was finalized together with my co-authors.

V I performed all calculations and wrote the first draft of the manuscript. The manuscript was finalized together with my co-author.

VI I performed all calculations and wrote the first draft of the manuscript. The manuscript was finalized together with my co-author.

PUBLICATIONS NOT INCLUDED IN THIS THESIS

Efficient parameterization of adsorbate–adsorbate interactions on metal surfaces
Willem Vanmoerkerke, Rasmus Svensson, and Henrik Grönbeck
Surf. Sci., **754**, 122678 (2025)

Skeletal editing by tip-induced chemistry
Shantanu Mishra, Valentina Malave, Rasmus Svensson, Henrik Grönbeck, Florian Albrecht, Diego Peña, and Leo Gross
J. Am. Chem. Soc., **147**, 44055–44059 (2025)

CO-induced structural flexibility in Cu and Au nano-catalysts
Rasmus Svensson, Alvaro Posada-Borbón, and Henrik Grönbeck
ChemCatChem, **18**, e01336 (2026)

Contents

1

Introduction

In a chemical reaction, reactants are transformed into products through processes involving the breaking and formation of bonds. Chemical reactions are reversible, and the net reaction occurs in the direction that minimizes the free energy of the system. For example, a reaction between hydrogen and oxygen, resulting in the formation of water, lowers the free energy, which is reflected by a large energy release. The large energy release means that the reverse reaction rate is negligible. However, despite the release of energy, the reaction does normally not occur at room temperature. For the reaction to occur, strong hydrogen-hydrogen and oxygen-oxygen bonds must be broken, which is associated with energy barriers. The higher the energy barrier is, the lower is the probability of the reaction to occur. One way of overcoming the energy barriers is to increase the temperature. However, this is energy intensive and can, in many cases, lead to undesirable side-reactions. Another way to increase the rate of a chemical reaction is by using a catalyst. In a catalytic reaction, the reactants interact with a catalyst material, resulting in altered reaction paths and energies upon the breaking and formation of the chemical bonds. The catalyst material is, ideally, not consumed in the process, and the energies of the reactants and products are not altered. The yields are therefore, in closed systems, limited by the thermodynamic equilibrium.

The catalytic acceleration of chemical reactions is crucial in many environmental and industrial processes, with applications ranging from the conversion and utilization of greenhouse gases [1–3] to the production of fuels and chemicals [4–7]. Catalysis is, depending on the catalyst and the reacting species, commonly divided into the three categories biocatalysis, homogeneous catalysis, and heterogeneous catalysis [8, p.5]. Biocatalysis concerns catalytic processes with biological materials, such as enzymes. In homogeneous catalysis, the phases of the catalyst and the

reactants are the same. A homogeneous catalyst could, for example, be a solvated metal atom, catalyzing a liquid reaction. In heterogeneous catalysis, the catalyst and the reacting molecules are in different phases; most commonly reactants in gas or liquid phase, catalyzed by a solid catalyst. Technological heterogeneous catalysts are often realized as metal nanoparticles supported on an oxide, operating under some specific reaction conditions. The efficiency of a catalyst is characterized with respect to:

- Activity – how much the reaction rates are increased,
- Selectivity – what the distribution of the products is, and
- Stability – how long it takes until the catalyst degrades.

Finding the optimal catalyst for a specific chemical reaction is generally challenging, as the performance depends on the elemental distribution and size of the metal nanoparticles, the choice of support, and the reaction conditions [9, 10].

1.1 Heterogeneous catalysis

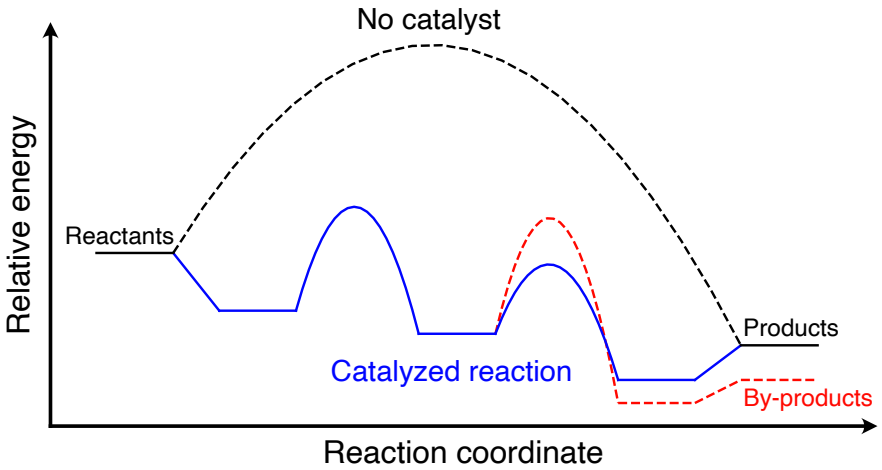

Figure 1.1: A schematic visualization of the influence of a catalyst on the energy changes in a chemical reaction. The dashed black line is the activation energy for the reaction in the absence of a catalyst. The solid blue line represents the catalyzed path towards the products, whereas the dashed red line leads to the formation of by-products.

A schematic visualization of how a catalyst may affect a chemical reaction is shown in Figure 1.1. In the absence of a catalyst, the energy barrier is high, and the reaction rate is low. In the presence of a solid catalyst, however, the overall reaction

is divided into a set of elementary reactions. First, the reacting species adsorb on the catalyst surface. Thereafter, processes involving the breaking and formation of chemical bonds occur, and the products desorb from the surface. An optimal catalyst should, therefore, bind reactants strongly enough so that the reaction can occur, but not too strongly, as to prevent undesirable bond-breaking and products sticking to the surface. This is known as the Sabatier principle [8, p.272–273]. In Figure 1.1, the blue pathway represents the catalyzed reaction towards the desired products. The overall reaction energy is the same as in the absence of a catalyst, but the energy barriers towards the products are decreased, and the reaction rate is therefore increased. However, on the catalyst surface, competing reactions could occur, forming undesirable by-products, visualized in red. This represents one of the challenges in heterogeneous catalysis. The catalyst should increase the rates towards the desired products, while keeping the rates towards the by-products low. A special case of undesired processes is the deactivation of the catalyst, resulting in a loss of activity. The deactivation could be a consequence of *e.g.*, catalyst degradation, or chemical changes to the catalyst surface [11].

1.2 Understanding catalytic reactions

Phenomenological understanding of catalytic reactions rates was obtained already in the end of the 1800's [8, p.24]. Catalytic reaction rates were deduced to follow the expression

$$r = k \prod_i [a_i]^{n_i}, \tag{1.1}$$

where k is a reaction rate constant, $[a_i]$ is the activity of the reactant, approximated as partial pressure or concentration, with corresponding reaction order n_i. Arrhenius found that the reaction rate constant scaled with temperature as

$$k = C\, \mathrm{e}^{-E_{\mathrm{app}}/k_{\mathrm{B}}T}, \tag{1.2}$$

where C is a constant factor, and E_{app} is the apparent activation energy of the entire reaction. Despite being deduced mainly from experimental measurements, with limited understanding of detailed catalytic processes, Eqs. (1.1) and (1.2) provide a description of the general behavior of catalytic reactions. However, to find suitable catalysts, and to optimize the systems with respect to activity, selectivity, and stability, atomic level understanding of the catalytic reactions is important.

The atomic understanding of catalytic reactions developed rapidly in the beginning of the 1900's. Theoretical description of adsorption processes on the catalyst surface and understanding of the underlying reaction mechanisms made it possible to quantitatively understand which processes might occur in catalytic reactions

[9, 12][8, p.24]. The mechanistic understanding did, however, not have a rigorous foundation until 1935, when Eyring combined quantum mechanics and statistical thermodynamics to predict the rates of elementary reactions based on the potential energy surface [13]. The conceptual understanding of catalytic reactions has since then developed in parallel with advancements of experimental techniques. X-ray diffraction made it possible to relate the performance of a catalyst to its crystalline structure [8, p.131]. Physical characterization of catalyst surfaces was enabled by *e.g.*, electron microscopy and low-energy electron diffraction methods [14, p.45], which was later refined to atomistic resolution with transmission electron microscopy and scanning tunneling microscopy [15]. The understanding of elemental distribution and the chemical state of the catalyst has been advanced by sensitive X-ray spectroscopy techniques [8, p.134–144], such as X-ray absorption spectroscopy and X-ray photoelectron spectroscopy [16]. It is also possible to obtain information of the intermediates present on the catalyst surface by *e.g.*, infrared spectroscopy [8, p.158], while the strength with which molecules are bound to the surface can be obtained from techniques such as micro-calorimetric measurements [8, p.289] or temperature-programmed desorption experiments [17, p.386–387].

Surface sensitive techniques are commonly used to probe well-defined catalysts in ultra-high vacuum conditions. However, industrial catalysts are often ill-defined and subject to harsher reaction conditions as compared to the model systems. This has led to the, so-called, materials and pressure gaps, which refer to the simplification of catalyst complexity and reaction conditions in model systems when surface sensitive experimental methods are used. Recently, methods to reduce these gaps have been developed, enabling the possibility to investigate different catalyst structures and chemical states also at liquid interfaces and at slightly elevated pressures [18–23]. However, the space and time-resolution of the experiments results in averaged behavior of the chemical processes on the surface. To aid in the interpretation of experimental results, and to guide in the optimization of new catalysts, computational models could be employed.

1.3 Computational approaches in catalysis

Computational catalysis relies on an accurate description of the changes in energy along a reaction path. For a long time such changes were challenging to obtain, due to the limited computational power, and the limited accuracy of the approximate solutions of the quantum mechanical equations. Early efforts were therefore targeted at understanding atomic and molecular adsorption processes. The description and understanding of adsorption on extended metal surfaces and clusters were in the 1960's developed thanks to *e.g.*, the Newns-Anderson model [24, 25] and

extended Hückel theory [26]. Around the same time, the foundations of density functional theory was formulated, in which the properties of systems are calculated from the electron density [27, 28]. This approach is less computationally expensive than, for example, the Hartree-Fock method. However, the accuracy of adsorption energies was low, and early focus was to calculate trends. As the efficiency and accuracy of density functional theory calculations increased in the 1990's [29, 30], it became possible to calculate adsorption energies on extended surfaces with reasonable accuracy. By comparing calculated adsorption energies with catalytic rate measurements, for example, the Sabatier principle could be rationalized by, so-called, volcano plots [8, p.273].

It is currently possible to calculate adsorption energies and activation energies for elementary reactions on extended surfaces and nanoparticles from first-principles, albeit at a high computational cost. The accurate description of the electronic structure for adsorption processes has enabled the possibility to understand and relate adsorption properties between different transition metal surfaces using simple descriptors [31–34]. Furthermore, by relating adsorption energies to elementary reaction energy barriers via *e.g.*, Brønsted-Evans-Polanyi relations [35], it is possible to explain trends in catalytic activity between different metals and geometries. However, to properly understand a catalytic reaction, and to obtain information of *e.g.*, the reaction mechanisms and possible kinetic bottlenecks, kinetic models are crucial.

With an accurate potential energy surface, it is possible to develop kinetic models based on first-principles data. In the mean-field approximation, the rate equations are solved analytically, based on the potential energy surface probed over model surfaces, *e.g.*, extended metal surfaces with specific orientation. This approach has provided great insight into the catalytic properties for many reactions on extended surfaces [36–44]. The mean-field approximation does, however, break down in the case of finite and inhomogeneous systems, or if substantial adsorption-adsorption interactions are present [45]. Modeling catalytic reactions over finite and inhomogeneous systems, such as nanoparticles, is challenging due to the large variety of catalytic sites with different chemical properties. The situation is further complicated in the case of dilute alloys, in which metal atoms are dispersed in another metal host at low concentration. In this case, the chemical properties of the metals may be altered, and the interplay between reactions occurring on the different metal sites could give rise to altered kinetics. One possibility to account for inhomogeneities of the catalyst is to employ kinetic Monte Carlo simulations, in which catalytic paths are probed stochastically [46]. This approach has provided valuable insight into the reaction mechanisms and kinetic bottlenecks for a range of reactions in complex catalytic systems [47–59].

1.4 The complexity of heterogeneous catalysis

Technological catalysts are often realized as metal nanoparticles supported on an oxide, operating under some specific reaction conditions. However, in computational approaches, the potential energy surface is commonly mapped for extended metal surfaces in vacuum conditions. Whereas the influence of elevated pressures in gas phase can be described by thermodynamics, the situation is complicated in the presence of liquid solvents. The influence of a solvent on the adsorption energies of intermediates can be taken into account by *e.g.*, an implicit solvation model [60]. This may, however, not accurately describe the real energy landscape of the catalyst, as the solvent could also influence the reaction by competitive adsorption, or enabling new reaction pathways [61, 62]. Furthermore, by mapping the energy landscape over extended metal surfaces, it is often assumed that the support is inert, and does not affect the catalytic reaction. However, the support could in certain cases influence the potential energy surface by *e.g.*, straining the metal nanoparticles, form complex metal/oxide structures, or alter the metal as a result of charge transfer [63–65].

When the potential energy surface is sufficiently well described, kinetic models are often employed on static catalyst structures to predict the efficiency, and reveal the dominant reaction mechanisms and possible kinetic bottlenecks. It has, however, been shown that catalysts are highly dynamic, and the structure of nanoparticles responds sensitively to changes in reaction conditions [18, 66–68]. In the case of alloy particles, the elemental distribution of the surface has been found to change upon variations in the reaction conditions [19, 69]. Furthermore, upon CO adsorption on gold clusters supported on CeO_2, transient catalysts of single gold ad-atoms were reversibly formed [70], emphasizing that the working catalyst may in some cases only be formed and be stable at certain reaction conditions. Similar phenomena have been observed also for extended surfaces under elevated gas pressures, where atoms detach from the metal, forming ad-atom clusters on the metal surface [20, 71–73]. The transient catalyst structures upon changes in reaction environment could have significantly altered catalytic properties. Hence, describing the dynamic behavior of the catalyst during reactions could be the next step in the closing of the complexity gap between model and operational catalysts.

1.5 Direct synthesis of H_2O_2 from H_2 and O_2

Hydrogen peroxide (H_2O_2) is an important green chemical [74]. The applications of H_2O_2 range from paper and textile bleaching [75], wastewater treatment [76], to organic synthesis [74, 77]. H_2O_2 is mainly produced in large-scale facilities, via se-

quential reduction and oxidation of anthraquinones [74, 78]. The process can yield large quantities of H_2O_2, at the cost of energy-demanding extraction processes and the production of toxic wastes. A direct process, in which H_2O_2 is catalyzed without the inclusion of organic compounds, at the location of usage, has the potential to be environmentally friendly and cost-efficient [79]. The reaction is challenging, as the formation of OOH and H_2O_2 on the catalyst surface is directly competing with undesirable O – O bond breaking, resulting in the irreversible formation of thermodynamically favorable H_2O [80]. The direct formation of H_2O_2 at ambient temperatures over Pd nanoparticles in different solvents has been investigated extensively [44, 81–84]. Unfortunately, the high reactivity of Pd results in O – O bond scission and, consequently, the formation of H_2O.

A less reactive metal, such as Au, could be a suitable catalyst to obtain high selectivities towards H_2O_2. However, in this case, the nanoparticles are unable to adsorb and dissociate H_2, and the activity is low [85]. One approach is to change support material, as Au/support interface sites are sometimes associated with significantly altered catalytic properties [86, 87]. However, the increased reactivity at the Au/support interface could have negative consequences for the selectivity towards H_2O_2, as O – O bond breaking is facilitated [87]. Another approach that has shown to increase the efficiency of the direct formation of H_2O_2 is to alloy Au with Pd [88, 89]. In the dilute limit, where Pd atoms are dispersed in the surface of water-solvated Au nanoparticles, selectivities close to 100 % have been measured [90]. Understanding the mechanisms behind the high performance of dilute PdAu nanoparticles solvated in water could be important in the catalyst optimization for direct H_2O_2 synthesis, and potentially other hydrogenation reactions where high selectivities are important.

1.6 CO_2 hydrogenation to CH_3OH

Another important group of hydrogenation reactions is the conversion of CO_2 into valuable chemicals, such as methanol, which could be used as a fuel or chemical feedstock [91–95]. In the catalytic conversion of CO_2 to methanol, CO_2 is hydrogenated according to:

$$CO_2 + 3\,H_2 \rightleftharpoons CH_3OH + H_2O. \tag{1.3}$$

In contrast to the direct formation of H_2O_2, where one wants to preserve the O – O bond, in the synthesis of methanol a C – O bond must be broken. Many different catalysts have been investigated for the reaction, such as indium oxide-based catalysts [96–99], Cu/ceria [100] catalysts, and ZnO/ZrO_2 catalysts [101]. Industrially, the process relies on $Cu/ZnO/Al_2O_3$ catalysts, operating at temperatures between

200–300 °C and gas mixtures of $CO_2/CO/H_2$ at high partial pressures [102]. The inclusion of CO in the gas mixture increases the activity, as CO *e.g.*, removes inhibiting water on the catalyst surface via the water-gas shift reaction [103, 104]. The reason for the efficiency of the industrial catalyst, and the synergetic interplay between Cu and ZnO is debated, and has been attributed to processes occurring at the Cu/ZnO interface [105], ZnO-induced strain of the Cu nanoparticles [106], the formation of a ZnO overlayer over Cu [107], and the formation of a Cu-Zn alloy [108]. Understanding of the Cu/ZnO synergy could aid in the development of more efficient catalyst materials.

1.7 Objective of the thesis

The objective of this thesis is to elucidate catalytic processes at the atomic scale, by employing different computational techniques. Specifically, the synergetic interplay between different catalyst constituents in catalytic reactions are explored by density functional theory calculations and kinetic Monte Carlo simulations. A schematic overview of the investigated phenomena is presented in Figure 1.2. (I) The kinetic implications of metal/metal interplay in the direct formation of H_2O_2 from H_2 and O_2 over dilute PdAu nanoparticles is investigated. (II) As hydrogenation reactions are often performed in an aqueous solution, charge transfer processes occurring at the metal/water interface are explored, and the kinetic implications for the direct formation of H_2O_2 are elucidated. (III) To explore the dynamic behavior of PdAu nanoparticles, a kinetic Monte Carlo approach is developed to model the structural time-evolution in inert and reactive atmospheres. (IV) The influence of metal/oxide charge transfer upon the adsorption of H_2 is investigated, and the kinetic implications for the hydrogenation of CO_2 to methanol are explored. This thesis is partly based on the author's licentiate thesis [109].

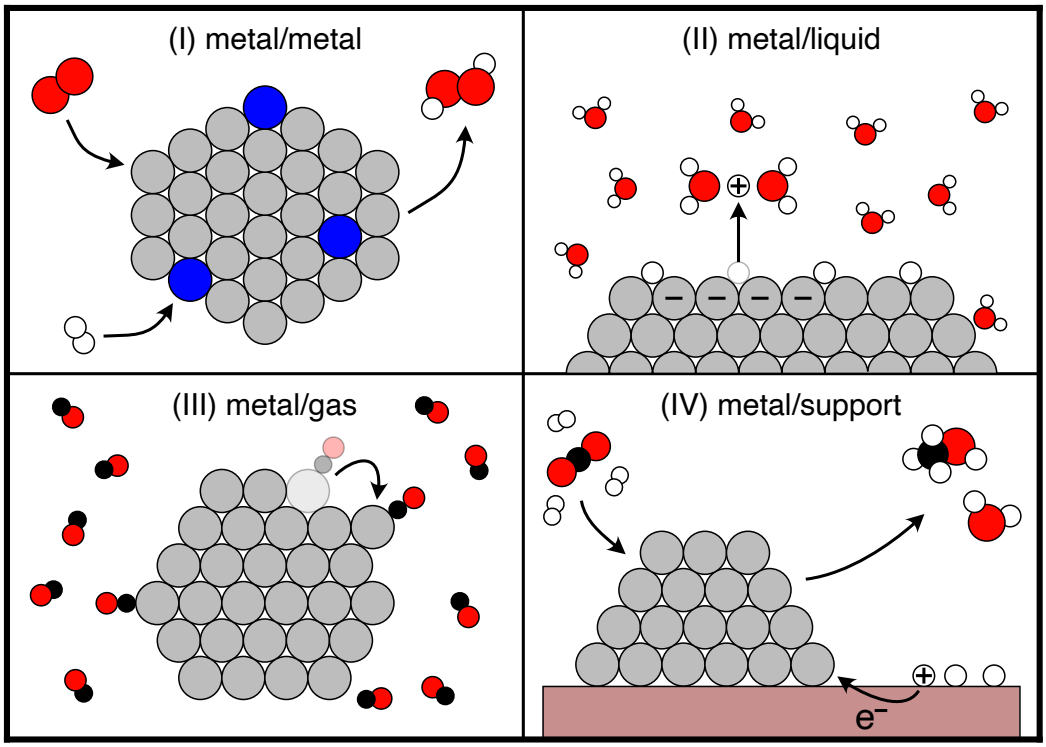

Figure 1.2: Schematic overview of the investigated processes and synergies. (I) Metal/metal interplay in the direct synthesis of H_2O_2. (II) Charge transfer processes at the metal/water interface. (III) Dynamic behavior of nanoparticles in a CO-atmosphere. (IV) Charge transfer phenomena at the metal/oxide interface, specifically for CO_2 hydrogenation to methanol.

2

The potential energy surface

Reaction kinetics, elementary reaction rates, and stability of intermediates are determined by the potential energy surface (PES). A chemical system in a specific atomic configuration corresponds to one point on the (ground state) PES. The PES is high-dimensional and complete knowledge of the surface is challenging to obtain, also for small systems. A two-dimensional PES is sketched in Figure 2.1.

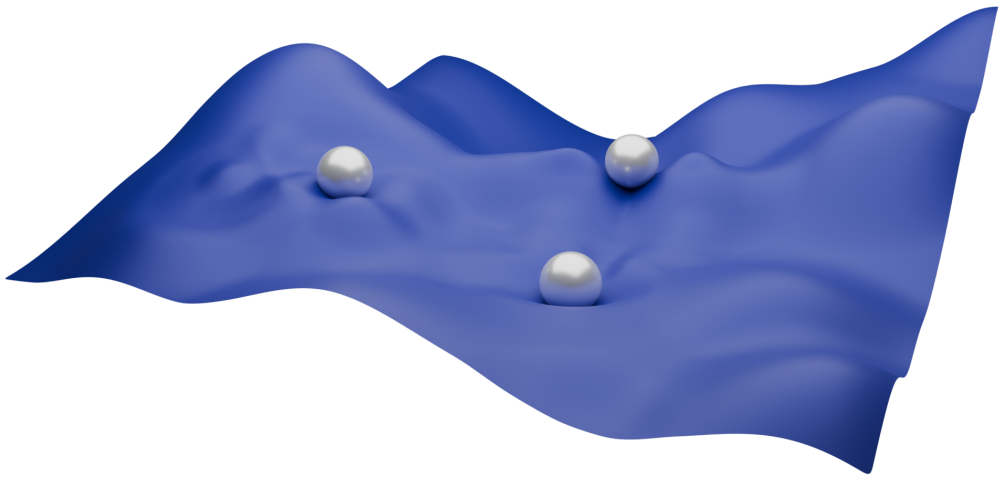

Figure 2.1: A two-dimensional potential energy surface. Three points on the PES, corresponding to a local minimum, the global minimum, and a saddle point, are highlighted with white balls.

On a catalyst surface, a stable intermediate configuration coincides with a local (or global) minimum on the PES. Upon an elementary reaction, transferring the system between two stable configurations, a transition state must be crossed, which corresponds to a first order saddle point on the PES.

Theory and methods to obtain information about the PES are presented in this chapter. First, density functional theory (DFT) is described, which is used to calculate the energy of a system in a specific atomic configuration. Thereafter, methods to propagate along the DFT-based PES, to find stable adsorption configurations, transition states, and entropic contributions, are presented. Lastly, methods to correlate the potential energies to stability and elementary reaction rate constants are reviewed.

2.1 One point on the potential energy surface

The total energy of a system in a specific atomic configuration can be calculated from quantum mechanics via the time-independent Schrödinger equation:

$$\hat{H}\Psi \;=\; E\Psi, \tag{2.1}$$

where $\hat{H}$ is the Hamiltonian operator, Ψ is the wavefunction, and E is the total energy of the system. In the absence of external fields, the Hamiltonian operator is the sum of the kinetic and electronic Coulomb potential energy operators:

$$\begin{aligned}\hat{H} &= \hat{T}_{\mathrm{e}} \;+\; \hat{T}_{\mathrm{N}} \;+\; \hat{V}_{\mathrm{ee}} \;+\; \hat{V}_{\mathrm{eN}} \;+\; \hat{V}_{\mathrm{NN}} \\ &= -\sum_i \frac{\hbar^2}{2m_{\mathrm{e}}}\nabla_i^2 \;-\; \sum_I \frac{\hbar^2}{2M_I}\nabla_I^2 \\ &+\; \frac{\mathrm{e}^2}{4\pi\varepsilon_0}\left(\sum_{i,\,j>i}\frac{1}{|\mathbf{r}_i-\mathbf{r}_j|} \;-\; \sum_{i,\,I}\frac{Z_I}{|\mathbf{r}_i-\mathbf{R}_I|} \;+\; \sum_{I,\,J>I}\frac{Z_I Z_J}{|\mathbf{R}_I-\mathbf{R}_J|}\right).\end{aligned} \tag{2.2}$$

Here, lowercase and uppercase letters are used to denote electrons and nuclei, respectively. The particles are in this case assumed to be point-like, non-relativistic, and spin-orbit coupling is neglected. [110, p.3–4]. As the potential energy operators couple the behavior of the particles, the dimensionality of the Schrödinger equation is difficult to reduce, and finding solutions requires approximations. A first step to reduce the dimensionality of the Schrödinger equation is the Born-Oppenheimer approximation.

2.1.1 The Born-Oppenheimer approximation

As the mass of an atomic nucleus is significantly greater than the mass of an electron, the motions of the nuclei and electrons can be decoupled. In the Born-Oppenheimer approximation, the electrons are assumed to remain in the same adiabatic eigenstate, and adjust instantaneously to deviations in the nuclear positions [111, p.8]. In this case, the total wavefunction can be approximated as the product between the nuclear and electronic wavefunctions. The electronic wavefunction, for the nuclear positions $\mathbf{R}_1, ..., \mathbf{R}_N$, is obtained from:

$$\hat{H}_{\mathrm{e}}\Psi_{\mathrm{e}}(\mathbf{R}_1, ..., \mathbf{R}_N; \mathbf{r}_1, ..., \mathbf{r}_n) \;=\; E_{\mathrm{e}}(\mathbf{R}_1, ..., \mathbf{R}_N)\Psi_{\mathrm{e}}(\mathbf{R}_1, ..., \mathbf{R}_N; \mathbf{r}_1, ..., \mathbf{r}_n), \quad (2.3)$$

where the electronic Hamiltonian operator is

$$\hat{H}_{\mathrm{e}} = \hat{T}_{\mathrm{e}} + \hat{V}_{\mathrm{ee}} + \hat{V}_{\mathrm{ext}}. \quad (2.4)$$

Here, $\hat{V}_{\mathrm{ext}}$ denotes the electron-nucleus Coulomb potential energy operator ($\hat{V}_{\mathrm{eN}}$ in Eq. (2.2)). The total energy of the system is in the case of static nuclei:

$$E = E_{\mathrm{e}} \;+\; E_{\mathrm{NN}}^{\mathrm{pot.}}, \quad (2.5)$$

where $E_{\mathrm{NN}}^{\mathrm{pot.}}$ is the Coulomb potential energy between the nuclei. For dynamical processes, the kinetic energy of the nuclei can be included by a classical description of the nuclear motion. The Born-Oppenheimer approximation is valid if the motions of the nuclei are slow, and the electronic energy levels are sufficiently separated.

The electronic Schrödinger equation is high-dimensional also after the Born-Oppenheimer approximation. An early approach to solve for the ground state electronic wavefunction and energy of a system was proposed by Hartree [112], in which the wavefunction was separated into one-electron wavefunctions, *i.e.*,

$$\Psi(\mathbf{r}_1, ..., \mathbf{r}_n) \approx \prod_i \psi_i(\mathbf{r}_i). \quad (2.6)$$

Each wavefunction was thereafter subject to a one-electron wave equation[1]

$$\Big(-\frac{1}{2}\nabla^2 + v_{\mathrm{ext}}(\mathbf{r}) + \bar{v}_{\mathrm{ee},i}(\mathbf{r})\Big)\psi_i(\mathbf{r}) = \varepsilon_i\psi_i(\mathbf{r}), \quad (2.7)$$

where v_{ext} is the external potential from the nuclei and $\bar{v}_{\mathrm{ee},i}$ is a mean Coulomb potential from all other electrons. The one-electron wavefunctions, which minimize

[1]Henceforth, atomic Hartree units are used, in which $m_{\mathrm{e}} = \mathrm{e} = \hbar = 4\pi\varepsilon_0 = 1$.

the total energy of the system, can in this way be obtained iteratively. A many-electron wavefunction must obey the Pauli exclusion principle. The total Hartree wavefunction obtained in Eq. (2.6) is, however, not antisymmetric with respect to the interchange of two electrons. To capture the fermionic nature of the electronic wavefunction, Fock proposed that the total wavefunction could instead be obtained from the determinant of the one-electron wavefunctions as [111, p.32]:

$$\Psi(\mathbf{r}_1\sigma_1, ..., \mathbf{r}_n\sigma_n) \approx \frac{1}{\sqrt{n!}} \begin{vmatrix} \psi_1(\mathbf{r}_1, \sigma_1) & \cdots & \psi_1(\mathbf{r}_n, \sigma_n) \\ \vdots & \ddots & \vdots \\ \psi_n(\mathbf{r}_1, \sigma_1) & \cdots & \psi_n(\mathbf{r}_n, \sigma_n) \end{vmatrix} \tag{2.8}$$

where σ is the spin of the electron.

2.1.2 The electron density

Another approach to solve for the ground state electronic energy was proposed by Thomas, Fermi, and Dirac. Instead of separating the total electronic wavefunction into one-electron wavefunctions, the electron density was utilized. Although an efficient way of reducing the dimensionality of the electronic Schrödinger equation, the kinetic energy of the electrons was poorly described by a density functional, approximated by a homogeneous electron gas [113, p.120–121]. Thus, the early attempts were not used in practical calculations. The approach to use the electron density as the basic parameter was put on a firm theoretical ground by Hohenberg and Kohn [27], showing that there is a one-to-one mapping (except for a constant term) between the external potential and the ground state electron density. Furthermore, it was shown that there exists a universal functional that maps the electron density to the electronic energy of the system, *i.e.*,

$$E[n(\mathbf{r})] = \int n(\mathbf{r}) v_{\text{ext}}(\mathbf{r})\, \mathrm{d}\mathbf{r} + F[n(\mathbf{r})] = E_{\text{ext}}[n(\mathbf{r})] + F[n(\mathbf{r})]. \tag{2.9}$$

The energy functional, E, obeys the variational principle, hence, it is minimized for the ground state electron density. The universal functional, F, can be separated into a functional accounting for the electron-electron interactions, and a functional G, so that

$$\begin{aligned} E[n(\mathbf{r})] &= E_{\text{ext}}[n(\mathbf{r})] + E_{\text{ee}}[n(\mathbf{r})] + G[n(\mathbf{r})] \\ &= \int n(\mathbf{r}) v_{\text{ext}}(\mathbf{r})\, \mathrm{d}\mathbf{r} + \frac{1}{2} \int n(\mathbf{r}) v_{\text{ee}}(\mathbf{r})\, \mathrm{d}\mathbf{r} + G[n(\mathbf{r})]. \end{aligned} \tag{2.10}$$

As the electron density is considered, the potentials have the forms:

$$v_{\text{ext}}(\mathbf{r}) = -\sum_k \frac{Z_k}{|\mathbf{r} - \mathbf{R}_k|} \tag{2.11}$$

$$v_{\text{ee}}(\mathbf{r}) = \int \frac{n(\mathbf{r}')}{|\mathbf{r}' - \mathbf{r}|}\, \mathrm{d}\mathbf{r}'. \tag{2.12}$$

The exact theory presented by Hohenberg and Kohn is, however, difficult to apply, as the theorems only prove the existence, and not the analytical form, of the universal functional F. An approach to apply the theory was developed by Kohn and Sham [28]. In the Kohn-Sham approach, G is replaced by a kinetic energy functional of non-interacting electrons T_0, and an exchange-correlation functional E_{xc}, that captures the effects that are neglected upon treating the electrons as non-interacting. Introducing single-particle Kohn-Sham orbitals, ψ, the kinetic energy functional is

$$T_0[n(\mathbf{r})] = -\frac{1}{2}\sum_i f_i \int \psi_i^*(\mathbf{r})\nabla^2\psi_i(\mathbf{r})\, \mathrm{d}\mathbf{r}, \tag{2.13}$$

where f_i is the electron occupation of the orbital. The total electron density in the system is obtained from

$$n(\mathbf{r}) = \sum_i f_i |\psi_i(\mathbf{r})|^2. \tag{2.14}$$

In the Kohn-Sham approach, the total electronic energy of the system is, hence,

$$E[n(\mathbf{r})] = E_{\text{ext}}[n(\mathbf{r})] + E_{\text{ee}}[n(\mathbf{r})] + T_0[n(\mathbf{r})] + E_{\text{xc}}[n(\mathbf{r})]. \tag{2.15}$$

The orbitals and the electron density are obtained in an iterative approach, from the Kohn-Sham equations:

$$\Big(-\frac{1}{2}\nabla^2 + v_{\text{eff}}(\mathbf{r})\Big)\psi_i(\mathbf{r}) = \varepsilon_i\psi_i(\mathbf{r}). \tag{2.16}$$

The effective potential $v_{\text{eff}}(\mathbf{r})$ is the sum of the external potential (Eq. (2.11)), the electron-electron potential (Eq. (2.12)), and the exchange-correlation potential, *i.e.*,

$$v_{\text{eff}}(\mathbf{r}) = v_{\text{ext}}(\mathbf{r}) + v_{\text{ee}}(\mathbf{r}) + v_{\text{xc}}(\mathbf{r}) \tag{2.17}$$

$$v_{\text{xc}}(\mathbf{r}) = \frac{\delta E_{\text{xc}}[n(\mathbf{r})]}{\delta n(\mathbf{r})}. \tag{2.18}$$

The kinetic energy of the system, $T_0[n(\mathbf{r})]$, is calculated from the Kohn-Sham eigenvalues, ε_i, as:

$$\begin{aligned} \sum_i f_i \int \psi_i^*(\mathbf{r})\varepsilon_i\psi_i(\mathbf{r})\,\mathrm{d}\mathbf{r} &= \sum_i f_i \int \psi_i^*(\mathbf{r})\Big(-\frac{1}{2}\nabla^2 + v_{\text{eff}}(\mathbf{r})\Big)\psi_i(\mathbf{r})\,\mathrm{d}\mathbf{r} \\ &\Longrightarrow \\ T_0[n(\mathbf{r})] &= \sum_i f_i\varepsilon_i - E_{\text{ext}}[n(\mathbf{r})] - 2E_{\text{ee}}[n(\mathbf{r})] - \int n(\mathbf{r})v_{\text{xc}}(\mathbf{r})\,\mathrm{d}\mathbf{r}. \end{aligned} \tag{2.19}$$

By inserting Eq. (2.19) into the total electronic energy functional (Eq.(2.15)), the total electronic energy is

$$E[n(\mathbf{r})] = \sum_i f_i\varepsilon_i - E_{\text{ee}}[n(\mathbf{r})] + E_{\text{xc}}[n(\mathbf{r})] - \int n(\mathbf{r})v_{\text{xc}}(\mathbf{r})\,\mathrm{d}\mathbf{r}. \tag{2.20}$$

For non-spin polarized calculations, each Kohn Sham-orbital can be occupied by two electrons ($f_i \leq 2$). The theory can be extended to also account for different spin states [111, p.64]. In this case, the total density is calculated as the sum of the two spin-densities. Each Kohn-Sham orbital can, in this case, be occupied by only one electron ($f_i \leq 1$) and the exchange-correlation functional is spin-dependent, *i.e.*,

$$v_{\text{xc}}(\mathbf{r},\sigma) = \frac{\delta E_{\text{xc}}[n(\mathbf{r},\sigma)]}{\delta n(\mathbf{r},\sigma)}. \tag{2.21}$$

The Kohn-Sham approach is an effective way of applying the density functional theory. However, as the approach assumes a system of non-interacting electrons, and an energy functional, E_{xc}, that should capture the discrepancy between the non-interacting and fully interacting systems, the accuracy heavily relies on the description of the exchange and correlation effects.

2.1.3 The exchange-correlation functional

The exchange and correlation functional should bridge the Kohn-Sham approach to the exact, fully interacting many-electron system. In the full system, the wavefunction must obey the Pauli exclusion principle. Another difficulty when considering the full many-electron wavefunction is the electronic correlation effects, resulting in changes to the kinetic energy contributions, as compared to the non-interacting system [111, p.66]. Furthermore, as the effective potential is calculated from the total electron density, each electron is, in the Kohn-Sham approach, interacting with itself. An early approach to approximate the exchange and correlation effects is the local density approximation (LDA) [111, p.77]. The electron density is described

as locally homogeneous and the exchange-correlation energy functional is:

$$E_{\mathrm{xc}}^{\mathrm{LDA}}[n(\mathbf{r})] = \int n(\mathbf{r})\varepsilon_{\mathrm{xc}}^{\mathrm{LDA}}[n(\mathbf{r})]\,\mathrm{d}\mathbf{r}. \tag{2.22}$$

The LDA is an exact description for a homogeneous electron gas, as $\varepsilon_{\mathrm{xc}}$ can be derived from quantum Monte Carlo simulations [114]. For open-shell systems, spin can be included in the LDA. In the local spin density approximation, the exchange and correlation energy functional of the two spin densities is

$$E_{\mathrm{xc}}^{\mathrm{LSDA}}[n_\uparrow(\mathbf{r}), n_\downarrow(\mathbf{r})] = \int n(\mathbf{r})\varepsilon_{\mathrm{xc}}^{\mathrm{LSDA}}[n_\uparrow(\mathbf{r}), n_\downarrow(\mathbf{r})]\,\mathrm{d}\mathbf{r}, \tag{2.23}$$

where $n(\mathbf{r}) = n_\uparrow(\mathbf{r}) + n_\downarrow(\mathbf{r})$. Albeit a reasonable approximation for *e.g.*, bulk metals and for determining the structure of systems with strong bonds, the L(S)DA approximation is poor for describing molecular bond strengths, metal surfaces, and other systems with highly varying densities [115] [111, p.82]. A way to enhance the performance of the exchange-correlation functional is to include a dependence on the electron density gradients. In the generalized gradient approximation (GGA), the exchange-correlation energy functional is expressed as:

$$\begin{aligned} &E_{\mathrm{xc}}^{\mathrm{GGA}}[n_\uparrow(\mathbf{r}), n_\downarrow(\mathbf{r})] \\ &= \int n(\mathbf{r})\varepsilon_{\mathrm{xc}}[n_\uparrow(\mathbf{r}), n_\downarrow(\mathbf{r})]F_{\mathrm{xc}}[n_\uparrow(\mathbf{r}), n_\downarrow(\mathbf{r}), \nabla n_\uparrow(\mathbf{r}), \nabla n_\downarrow(\mathbf{r})]\,\mathrm{d}\mathbf{r}, \end{aligned} \tag{2.24}$$

where F_{xc} is an enhancement functional to account for density inhomogeneities. Many GGA functionals have been developed [116–120], either to follow physical constraints, or to better reproduce experimental observations.

In addition to chemical bonds, dispersion interactions could be important for adsorbed molecules. Dispersion interactions do not stem from density overlap or chemical bond, but rather electric field coupling from density fluctuations. The interactions are long-ranged and are, therefore, not effectively captured by LDA or GGA [110, p.228–230]. Exchange-correlation functionals accounting for dispersion interactions have been developed [121–123]. Dispersion interactions can also be accounted for without explicit description in the E_{xc} functional. A parametrized dispersion energy, based on the position of the nuclei is, in the D3-method, added to the ground state energy after the Kohn-Sham equations have been solved [124].

Exchange-correlation functionals tend to poorly describe the electron self-interaction correction, resulting in an over-delocalization of electrons [113, p.160–161]. This problem is most emphasized in systems with strongly correlated d and f electrons,

such as metal-oxides [125]. The description can be improved by employing a hybrid functional [111, p.96][126], in which the description of the exchange effects is a combination between density functionals and Hartree-Fock calculated contributions as:

$$E_{\mathrm{xc}} = \alpha E_{\mathrm{x}}^{\mathrm{HF}} + (1-\alpha)E_{\mathrm{x}}^{\mathrm{DFT}} + E_{\mathrm{c}}^{\mathrm{DFT}}, \tag{2.25}$$

where $\alpha \in (0,1)$. Hybrid functionals are computationally expensive and therefore unsuitable for large systems. Another approach to improve the description of strongly correlated systems is by including a Hubbard U-correction, which compensates for the electron self-interaction [127].

2.1.4 Solving the Kohn-Sham equations

Calculations for periodic systems, such as extended metal or metal-oxide surfaces, are greatly simplified by Bloch's theorem, which states that a wavefunction subject to a periodic external potential can be expressed as [113, p.88]:

$$\psi_{\mathbf{k}}(\mathbf{r}) = \mathrm{e}^{\mathrm{i}\mathbf{k}\cdot\mathbf{r}} u_{\mathbf{k}}(\mathbf{r}), \tag{2.26}$$

where u has the same periodicity as the external potential. The periodicity of the potential can be expressed by three vectors: $\mathbf{a}_1$, $\mathbf{a}_2$, and $\mathbf{a}_3$. From these vectors, the reciprocal lattice vectors are defined as

$$\mathbf{b}_i = \frac{2\pi\, \mathbf{a}_j \times \mathbf{a}_k}{\mathbf{a}_1 \cdot (\mathbf{a}_2 \times \mathbf{a}_3)}. \tag{2.27}$$

The volume spanned within the reciprocal lattice vectors is the Brillouin zone. All other vectors in reciprocal space can be expressed as the sum of a specific vector in the Brillouin zone and a vector $\mathbf{G} = n_1\mathbf{b}_1 + n_2\mathbf{b}_2 + n_3\mathbf{b}_3$, where n_1, n_2, and n_3 are integers. To sample the reciprocal space, a plane wave basis set can be utilized. The basis set is defined as

$$\phi_{\mathbf{k},\mathbf{G}}(\mathbf{r}) = \frac{1}{\sqrt{|\mathbf{a}_1 \cdot (\mathbf{a}_2 \times \mathbf{a}_3)|}} \mathrm{e}^{\mathrm{i}(\mathbf{k}+\mathbf{G})\cdot\mathbf{r}}. \tag{2.28}$$

As the Kohn-Sham orbital, ψ, is periodic, it can be expressed as a Fourier series of the basis set according to

$$\psi_{i,\mathbf{k}}(\mathbf{r}) = \sum_{G} C_{i,\mathbf{k}}(\mathbf{G})\phi_{\mathbf{k},\mathbf{G}}(\mathbf{r}). \tag{2.29}$$

In reciprocal space, the Kohn-Sham equations have the form [111, p.184]

$$\sum_{\mathbf{G}'} \Big(\frac{1}{2}|\mathbf{k}+\mathbf{G}|^2\delta_{\mathbf{G},\mathbf{G}'} + \tilde{v}(\mathbf{G}-\mathbf{G}')\Big) C_{i,\mathbf{k}}(\mathbf{G}') = \varepsilon_{i,\mathbf{k}} C_{i,\mathbf{k}}(\mathbf{G}), \tag{2.30}$$

where $\tilde{v}$ is the Fourier transform of the Kohn-Sham effective potential. As the Fourier coefficients decrease rapidly with $\mathbf{G}$, the expansion is usually truncated at a specific cutoff energy value:

$$\frac{1}{2}|\mathbf{k}+\mathbf{G}|^2 < E_{\text{cut.}}. \tag{2.31}$$

It is also possible to truncate the sampling of the Brillouin zone (number of $\mathbf{k}$) in the calculations. However, the truncation has to be determined from explicit testing as to when *e.g.*, the cohesive energy or specific adsorption energies are converged. After the Kohn-Sham orbitals have been obtained for each $\mathbf{k}$-point, the total electron density is obtained as

$$n(\mathbf{r}) = \sum_{\mathbf{k}} w_{\mathbf{k}} \sum_{i} f_{i,\mathbf{k}} |\psi_{i,\mathbf{k}}(\mathbf{r})|^2, \tag{2.32}$$

where w is a weight factor of the $\mathbf{k}$-point and f is the occupancy of the orbital. The plane wave approach is an efficient method for periodic systems with smoothly varying potentials; especially, the kinetic energy is simple to evaluate. However, for periodic systems with a net charge, such as a negatively charged metal surface, the electronic potential energy diverges at $\mathbf{G} = \mathbf{0}$. This can be compensated by the inclusion of an equally charged uniform background (jellium) [128]. As the background charge is uniform, the Fourier transform compensates for the divergence at $\mathbf{G} = \mathbf{0}$.

In the case of strongly oscillating wavefunctions, a very large number of plane waves are required to accurately describe their behavior. The oscillations are most significant close to the atomic nuclei. One approach to get around this problem, is by employing the projector-augmented wave (PAW) method [129]. In the PAW method, the solutions for the spherical Schrödinger equation for the *single atoms* with varying energy eigenvalues and angular momenta are determined. This set is denoted as the target set $|\phi_j\rangle$. For the chemical system of interest, consisting of either one or more atoms, an augmentation sphere is defined symmetrically around each atom. A set of smoother, orthogonal, pseudo-wavefunctions $|\tilde{\phi}_j\rangle$ is formulated, satisfying

$$|\phi_j\rangle = \mathcal{T}\,|\tilde{\phi}_j\rangle = |\tilde{\phi}_j\rangle + \sum_i \left(|\phi_i\rangle - |\tilde{\phi}_i\rangle \right) \langle \tilde{p}_i|\tilde{\phi}_j\rangle\,, \tag{2.33}$$

where $\langle \tilde{p}_i|$ is a local projector in the augmentation sphere satisfying $\langle \tilde{p}_i|\tilde{\phi}_j\rangle = \delta_{ij}$. Notice that the augmentation depends on the atomic specie, and angular momentum quantum numbers. After the pseudo-wavefunctions have been converged, with respect to the Hamiltonian $\tilde{H} = \mathcal{T}^\dagger H \mathcal{T}$, the orbital wavefunctions can be determined from

$$|\psi_n\rangle = |\tilde{\psi}_n\rangle + \sum_i \left(|\phi_i\rangle - |\tilde{\phi}_i\rangle \right) \langle \tilde{p}_i|\tilde{\psi}_n\rangle\,. \tag{2.34}$$

The orbital wavefunction is, hence, corrected within each augmentation sphere with the exact atomic wavefunctions. This can be done for all electrons in the system. However, as core electrons are not significantly involved in the forming and breaking of bonds, they are assumed to be frozen, also outside of the augmentation sphere, *i.e.* represented by the wavefunctions calculated for the single atoms [130].

2.2 Exploring the potential energy surface

With the density functional theory calculations presented this far, it is possible to calculate the energy of a chemical system in a specific nuclear configuration, *i.e.*, one point on the potential energy surface. In this section, methods to find local minima and first-order saddle points on the PES are presented. These points are of considerable interest, as minima correspond to stable intermediate configurations, and first-order saddle points correspond to transitions state configurations.

2.2.1 Finding local minima

To find, *e.g.*, stable adsorption configurations and stable nanoparticle structures, minima in the PES with respect to nuclear positions must be obtained. It is possible, with a converged electron density, to find the forces acting on each nucleus from the electron density [131]. The Hellmann-Feynman force on a nucleus in the system is

$$F_i = -\nabla_i E = -\nabla_i E_{\mathrm{NN}}^{\mathrm{pot.}} \; - \int \Psi_{\mathrm{e}}^{*}(\mathbf{r}) \nabla_i (\hat{H}_{\mathrm{e}}) \Psi_{\mathrm{e}}(\mathbf{r}) \, \mathrm{d}\mathbf{r}. \tag{2.35}$$

For local potentials, the second term becomes an expression that only depends on the electron density:

$$F_i = -\nabla_i E_{\mathrm{NN}}^{\mathrm{pot.}} - \int n(\mathbf{r}) \nabla_i v_{\mathrm{ext}}(\mathbf{r}) \, \mathrm{d}\mathbf{r}. \tag{2.36}$$

The unperturbed electron density can be used, as the effects on the kinetic energy of the electrons and the electron-electron interactions upon deviations of nuclear motion cancel [113, p.57]. When the forces on each nuclei have been determined, the structure can be updated by moving the nuclei along the forces.

2.2.2 Vibrational modes

Atoms and molecules bound to a catalyst surface vibrate with characteristic frequencies. The energy of a vibration is quantized according to

$$E_n = h\nu \left(\frac{1}{2} + n \right), \quad n = 0, 1, 2... \tag{2.37}$$

where ν is frequency of the vibrational mode. Owing to Heisenberg's uncertainty principle, the system cannot reside in the bottom of the potential energy well [132, p.20–21]. The lowest energy state for a specific atomic configuration must therefore include the zero-point energy contribution

$$E_{\text{zpc}} = \frac{1}{2}\sum_i h\nu_i, \tag{2.38}$$

where the summation is performed over the frequencies corresponding to the vibrational modes. Furthermore, the frequencies give important insight into the chemical system. For example, for an adsorbate in a local minimum, all frequencies are positive, whereas at the transition state, exactly one frequency is imaginary. In this work, the frequencies have been calculated assuming the harmonic approximation, *i.e.*, the PES in the vicinity of the configuration of interest is assumed to be quadratic. Upon finite movements of the atoms, a mass-weighted Hessian matrix is constructed. The frequencies of the different modes are thereafter obtained from the eigenvalues of the Hessian, λ_i, as $\nu_i = \sqrt{\lambda_i}/(2\pi)$.

2.2.3 Finding transition state configurations

An elementary catalytic reaction, transferring the system from one configuration to another, corresponds to the transition between two local minima in the PES. On the catalyst surface, the reaction can occur in many different ways. The most facile reaction path contains the lowest energy barrier. The transition state configuration for the most facile reaction path is therefore obtained from the highest point in the lowest energy path. The transition state is, hence, a first-order saddle point in the PES. Several different methods can be applied to obtain transition state configurations, where the nudged elastic band method [133] and the dimer method [134] are two examples. To find first-order saddle points, the structure must propagate according to the forces along all coordinates, except along the reaction coordinate, where the energy should be maximized. Hence, the "forces" on each atom i towards the transition state are given by

$$F_i^{\text{saddle}} = -\nabla_i E + 2\nabla_i E \cdot \hat{\tau}_i\,\hat{\tau}_i, \tag{2.39}$$

where $\hat{\tau}_i$ is the reaction coordinate for the specific nucleus. In the nudged elastic band method, the reaction coordinates are obtained from defining a set of intermediate structures, interpolated between the initial and final state configurations. Between each intermediate, springs are added along the reaction coordinates, hence, iteratively defining the reaction coordinates. However, as this approach only provides the reaction path, the spring forces are, in the climbing-image nudged elastic band method, added to all intermediate structures except for the highest energy one, to find the correct transition state configurations [135].

2.2.4 Molecular dynamics simulations

In cases for very dynamic systems with many close-lying minima on the PES, molecular dynamics (MD) simulations can be employed to find stable intermediate configurations. MD can, for example, be employed for processes at the metal/water interface, where the configuration space of the water molecules is large, and slight distortions to the structure result in significant changes in energy. In classical MD simulations, Newton's equations of motion are integrated, propagating the chemical system in time according to *e.g.*, the leap-frog algorithm [136, p.80]:

$$\mathbf{v}_i\Big(t+\frac{\Delta t}{2}\Big) = \mathbf{v}_i\Big(t-\frac{\Delta t}{2}\Big) + \frac{\mathbf{F}_i}{m_i}\Delta t \tag{2.40}$$

$$\mathbf{r}_i\Big(t+\Delta t\Big) = \mathbf{r}_i(t) + \mathbf{v}_i\Big(t+\frac{\Delta t}{2}\Big) \tag{2.41}$$

$$\mathbf{v}_i(t) = \frac{1}{2}\left(\mathbf{v}_i\Big(t+\frac{\Delta t}{2}\Big) + \mathbf{v}_i\Big(t-\frac{\Delta t}{2}\Big)\right). \tag{2.42}$$

In *ab initio* MD, the atomic velocities are updated according to the forces obtained from DFT calculations. The approach is an effective way of sampling larger parts of the configurational space. However, MD simulations will, to a large extent, sample configurations close to local minima, and hence, cannot be used to explore transition state configurations. To more efficiently sample rare events, constraints, such as the bond length between two atoms, can be included in the simulations. If constraints are included, an additional term is added to the DFT-calculated forces, so that the total force on each atom is [137]:

$$\mathbf{F}_i = -\nabla_i E - \sum_k \lambda_k(t)\nabla_i\sigma_k(t), \tag{2.43}$$

where the first term is the force due to the PES, and the second term is a summation over all constraints in which the atom is involved. The constraint σ, and the corresponding Lagrange multiplier λ, are time-dependent, and can therefore be updated during the simulation to *e.g.*, represent the elongation of a specific bond. As a result of the heavy sampling of the PES when performing MD simulations, the entropic changes can be captured and included in the exploration of events. The free energy difference along the reaction coordinate ξ in constrained MD simulations can be evaluated from thermodynamic integration [138]

$$A(\xi_1) - A(\xi_0) = \int_{\xi_0}^{\xi_1} \left(\frac{\partial A}{\partial \xi'}\right) \mathrm{d}\xi'. \tag{2.44}$$

The derivative of the free energy along the reaction coordinate can be calculated at different points from the statistical average [138, 139]

$$\frac{\partial A}{\partial \xi'} = \frac{\left\langle B_1^{-1/2}[-\lambda + k_\mathrm{B}TB_2]\right\rangle_{\xi'}}{\left\langle B_1^{-1/2}\right\rangle_{\xi'}}, \tag{2.45}$$

where λ is the Lagrange multiplier of the specific constraint and B_1 and B_2 are functions of the reaction coordinate and the atomic masses:

$$\begin{aligned} B_1 &= \sum_i \frac{1}{m_i} \nabla_i \xi \cdot \nabla_i \xi \\ B_2 &= \frac{1}{Z^2} \sum_{i,j} \frac{1}{m_i m_j} \nabla_i \xi \cdot (\nabla_i \nabla_j \xi) \cdot \nabla_j \xi. \end{aligned} \tag{2.46}$$

The constrained MD approach is convenient if the system is highly dynamic, and transition state configurations are difficult to obtain, *e.g*, for events occurring at the interface between a metal surface and an aqueous solution.

2.3 From potential energy surface to reaction rate constants

From the methods presented in the previous sections, it is possible to get an understanding of the potential energies in catalytic processes. However, to explore the reaction kinetics, including *e.g.*, elementary reaction rates, dominant reaction paths, and rate-determining steps, the knowledge of the PES must be translated into elementary rate constants, which is done via partition functions.

2.3.1 Partition functions

The partition function, Z, for a specific chemical system in thermal equilibrium with its surroundings, where energy is allowed to be exchanged, is defined as

$$Z = \sum_i g_i \mathrm{e}^{-E_i/k_\mathrm{B}T}. \tag{2.47}$$

The summation is performed over all energy states, and g is the degeneracy of the state. The partition function could, in principle, be obtained from complete potential energy sampling [140]. However, for intermediates bound to a catalyst surface, the contribution to the partition function is often approximated as stemming from

only vibrational degrees of freedom (with the bottom of the potential energy well as reference), *i.e.*,

$$Z = Z_{\text{vib.}} = \prod_i \sum_{n=0}^{\infty} \mathrm{e}^{-h\nu_i\left(n+\frac{1}{2}\right)/k_{\mathrm{B}}T} = \mathrm{e}^{-\sum_i h\nu_i/2k_{\mathrm{B}}T} \prod_i \frac{1}{1-\mathrm{e}^{h\nu_i/2k_{\mathrm{B}}T}}, \tag{2.48}$$

where the first factor corresponds to the zero-point energy correction. In cases where the approximation of only vibrational contributions cannot be made, the partition function is instead obtained from the assumption that translational, rotational, and vibrational degrees of freedom are decoupled, so that

$$Z \approx Z_{\text{tr.}} Z_{\text{rot.}} Z_{\text{vib.}}. \tag{2.49}$$

The partition function has additional contributions from electronic and nuclear effects, however, they are often set to unity. The translational partition function is derived from non-interacting particles, confined in an N-dimensional box with lengths L_i, resulting in:

$$Z_{\text{tr.}} = \left(\frac{\sqrt{2\pi m k_{\mathrm{B}}T}}{h}\right)^N \prod_{i=1}^{N} L_i, \tag{2.50}$$

where $N = 3$ for a freely translating molecule in gas phase. Depending on the rotational degrees of freedom, the partition function is given by [141, p.82]:

$$\begin{aligned} Z_{\text{rot.}}^{\text{1D}} &= \frac{2\pi}{h}\sqrt{2\pi I k_{\mathrm{B}}T} \\ Z_{\text{rot.}}^{\text{2D}} &= \frac{8\pi^2 I k_{\mathrm{B}}T}{\sigma h^2} \\ Z_{\text{rot.}}^{\text{3D}} &= \frac{\sqrt{\pi}}{\sigma}\prod_i \sqrt{\frac{8\pi^2 I_i k_{\mathrm{B}}T}{h^2}}, \end{aligned} \tag{2.51}$$

where I is the moment of inertia, I_i are the eigenvalues of the matrix of moments of inertia, and σ is a factor accounting for the symmetry of the system. The probability of a chemical system in equilibrium being in a specific energy state s, with energy $E(s)$ is given by the Boltzmann distribution [142, p.229]:

$$P(s) = \frac{g(s)\mathrm{e}^{-E(s)/k_{\mathrm{B}}T}}{Z}. \tag{2.52}$$

2.3.2 Transition state theory

The rate constant for an elementary reaction can be derived from the partition functions of the initial and transition state configurations. The rate constant is given by the probability of the specie being in the transition state with respect to the initial state via a quasi-equilibrium, and the vibrational frequency along the reaction coordinate [13]:

$$k = \nu \frac{Z^{\ddagger}}{Z_{\text{ini}}}. \tag{2.53}$$

The vibrational contribution to the partition function along the reaction coordinate can be extracted from the partition function at the transition state, *i.e.*,

$$k = \nu \frac{\mathrm{e}^{-h\nu/2k_{\text{B}}T}}{1-\mathrm{e}^{-h\nu/k_{\text{B}}T}} \frac{Z^{\ddagger *}}{Z_{\text{ini}}}. \tag{2.54}$$

If $k_{\text{B}}T >> h\nu$, the rate constant becomes

$$k \approx \frac{k_{\text{B}}T}{h} \frac{Z^{\ddagger *}}{Z_{\text{ini}}}. \tag{2.55}$$

The potential energy of the transition state and initial state configurations can thereafter be extracted from the partition functions, resulting in

$$k \approx \frac{k_{\text{B}}T}{h} \frac{Z_0^{\ddagger,*}}{Z_{\text{ini},0}} \mathrm{e}^{-\Delta E^{\ddagger}/k_{\text{B}}T}, \tag{2.56}$$

where the subscript 0 indicates that $\Delta E^{\ddagger}$ is measured from the bottom of the potential energy wells.

2.3.3 Adsorption rates

A special case of elementary reactions is the adsorption of a molecule on a catalyst surface. In this case, the partition function of the initial state is the gas phase partition function. The partition function of the transition state, excluding the reaction coordinate, can be approximated as a free gas molecule with one translational degree of freedom removed. The rate constant for adsorption events can, therefore, be expressed as

$$k_{\text{ads.}} = \frac{k_{\text{B}}T}{h} \frac{Z^{\text{2D}}}{Z^{\text{3D}}} \mathrm{e}^{-\Delta E^{\ddagger}/k_{\text{B}}T} = \frac{pa}{\sqrt{2\pi m k_{\text{B}}T}} \mathrm{e}^{-\Delta E^{\ddagger}/k_{\text{B}}T}, \tag{2.57}$$

where the last equality is a result of Eq. (2.50) and the ideal gas law. Here, p is the partial pressure of the gas, and a is the area of the adsorption site. Often, a sticking coefficient s is included in the rate constant, to account for *e.g.*, non-adiabatic electronic effects neglected in the Born-Oppenheimer approximation [143].

2.3.4 Free energies

Elementary reactions are highly reversible, especially when close to equilibrium conditions. If the rate constant of a specific elementary reaction is denoted k^+, the reverse reaction rate constant, k^-, can, according to Eq. (2.55) and the shared transition state, be expressed as:

$$k^- = \frac{Z_{\text{ini}}}{Z_{\text{fin}}} k^+. \tag{2.58}$$

For a reaction occurring with a fixed number of particles (N), constant volume (V), and constant temperature (T), it is convenient to work with Helmholtz free energy, A. It is related to the partition function as [142, p.248]

$$A = E - TS = -k_{\text{B}} T \ln Z, \tag{2.59}$$

where the entropy S is obtained from

$$S = -\left(\frac{\partial A}{\partial T}\right)_{N,V} = \frac{\partial}{\partial T}\left(k_{\text{B}} T \ln Z\right)_{N,V}. \tag{2.60}$$

As A scales monotonically with Z, changes in Helmholtz free energy will govern the stability of intermediates and the kinetics of the reaction. If the pressure p is kept constant, instead of the volume, extra compressive/expansive work is required. In this case, the reaction is governed by changes in Gibbs free energy:

$$\Delta G = \Delta A + p\Delta V = \Delta E + p\Delta V - T\Delta S. \tag{2.61}$$

The reaction rate constant and reverse reaction rate constant for a specific elementary reaction, can in a constant NPT system be expressed as

$$k^+ = \frac{k_{\text{B}} T}{h} \mathrm{e}^{-\Delta G^\ddagger / k_{\text{B}} T} \tag{2.62}$$

$$k^- = k^+ \mathrm{e}^{\Delta G / k_{\text{B}} T}, \tag{2.63}$$

where $\Delta G^\ddagger$ is the free energy barrier of the elementary reaction, and ΔG is the elementary reaction free energy. By describing the reverse reaction rate constant from the forward reaction rate constant and the elementary reaction free energy, thermodynamic consistency is maintained. It should be emphasized that $\Delta G^\ddagger$ and ΔG are not constant, but depend on the temperature, partial pressures, and local environments on the catalyst surface.

3

First-principles-based kinetic modeling

With the methods presented in Chapter 2, the rate constants for different elementary reactions can be calculated from first principles. The potential energy surface and the elementary reaction rate constants can give insight into the catalytic reaction. However, kinetic modeling is crucial to properly understand the reaction mechanism and possible kinetic bottlenecks. In first-principles-based kinetic modeling, the free energies are used to probe the time-evolution of a chemical system.

As an example, consider the reaction $\mathrm{A(g)} + \mathrm{B(g)} \rightleftharpoons \mathrm{AB(g)}$. On the catalyst surface, the reaction is separated into a set of elementary reactions, visualized in Figure 3.1. The adsorption and desorption of reactants A and B are indicated with red and blue arrows, respectively. Diffusion on the surface is visualized with black arrows. The reaction between A and B, forming AB is represented with a green arrow. When AB is formed, it desorbs from the surface, shown with a purple arrow. However, more processes could occur on the surface, such as the formation and desorption of an undesirable by-product, for example, $\mathrm{AB_2}$.

In this chapter, kinetic theory and methods to investigate the time-evolution of catalytic systems are presented. The foundations of mean-field kinetic modeling and kinetic Monte Carlo simulations are reviewed, and the different approaches are compared. The chapter is concluded with a section on kinetic data analysis, and how the results can be related to experimental observations.

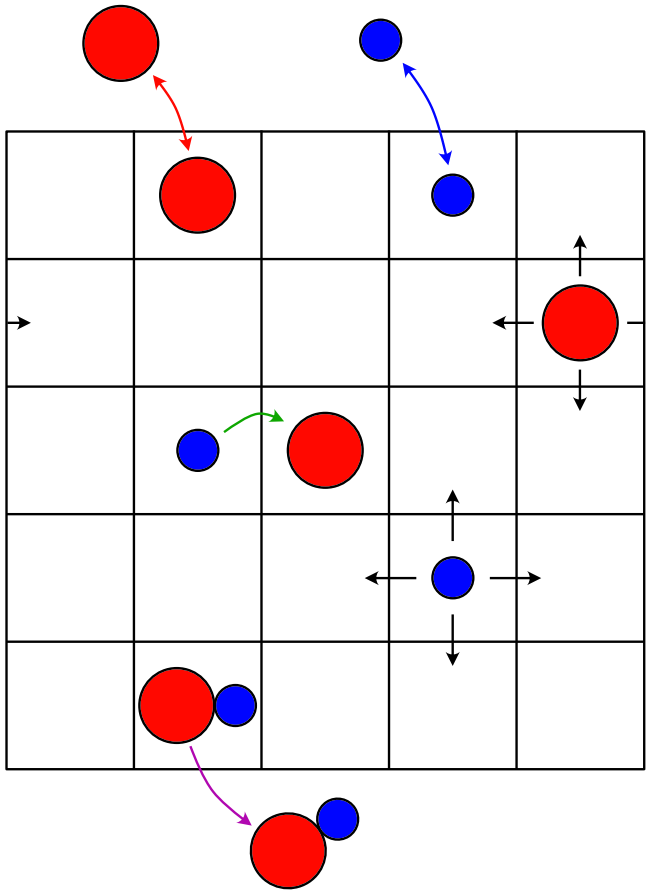

Figure 3.1: A schematic overview of possible events occurring in the reaction $\mathrm{A(g) + B(g) \rightleftharpoons AB(g)}$. The red and blue arrows indicate the adsorption and desorption of A and B, respectively. Black arrows show diffusion on the surface, whereas the green arrow represents the formation of AB. When AB is formed, it can desorb from the surface, visualized with a purple arrow.

3.1 The chemical master equation

The adsorbate-configuration presented in Figure 3.1, is one of many possible states that the surface may be in. Upon an elementary reaction, a new state is obtained. In the case of no surface symmetries, the number of states scales exponentially with the number of surface sites. The configurational space is, hence, enormous and complete sampling of all states is not feasible. It is therefore important to apply methods to explore the states in systematic ways. The chemical master equation describes the change in probability of a specific state i, with respect to

time [144, 145]:

$$\frac{\mathrm{d}P_i}{\mathrm{d}t} = \sum_j \Big(W_{ij} P_j - W_{ji} P_i \Big). \tag{3.1}$$

P is the probability of the specific state and the summation is performed over all other states. The first part in the summation represents the transition from state j to state i with the corresponding rate W_{ij}, wheres the second part is the transition from state i to state j with the corresponding transition rate W_{ji}. It should be noted that the majority of possible states are not directly connected, as there are no elementary reactions transferring the system between the states. The transition rates W_{ij} are for these transitions zero.

3.2 Mean-field kinetic modeling

From Eq. (3.1) it is, in simple cases, possible to derive analytic expressions for the surface coverages and reaction rates. The expectation value of the number of adsorbed A on the catalyst surface is

$$\langle \mathrm{A} \rangle = \sum_i P_i \mathrm{A}_i, \tag{3.2}$$

where P_i is the probability of the state and A_i is the number of A in the specific state. The change of the expectation value of the number of adsorbed A is

$$\frac{\mathrm{d}\langle \mathrm{A} \rangle}{\mathrm{d}t} = \sum_i \frac{\mathrm{d}P_i}{\mathrm{d}t} \mathrm{A}_i = \sum_i \left(\sum_j \Big(W_{ij} P_j - W_{ji} P_i \Big) \right) \mathrm{A}_i = \sum_{i,j} W_{ij} P_j (\mathrm{A}_i - \mathrm{A}_j). \tag{3.3}$$

Here, $(\mathrm{A}_i - \mathrm{A}_j)$ represents the change of number of adsorbed A upon the transition from state j to state i. This value depends on the specific elementary reaction, and is zero in the case of diffusion on the surface. Under the assumption that all surface sites are equal and no adsorbate-adsorbate interactions are present, the transition rates upon an elementary reaction $\mathrm{A} + \mathrm{B} \rightarrow \mathrm{AB}$, are all equal to an elementary rate constant k. Assuming that A and B may react to form one AB-configuration, if they occupy neighboring surface sites, the change in expectation value of A upon the elementary reaction is

$$\frac{\mathrm{d}\langle \mathrm{A} \rangle}{\mathrm{d}t} = -\sum_{i,j} W_{ij} P_j = -k \sum_j P_j \, (\mathrm{A} - \mathrm{B})_j^{\text{neighbors}} = -k \langle (\mathrm{A} - \mathrm{B})^{\text{neighbors}} \rangle. \tag{3.4}$$

$(\mathrm{A} - \mathrm{B})_j^{\text{neighbors}}$ is the number of possible final states i from each initial state j. The probability of a specific A and a specific B occupying neighboring sites on the

surface is

$$p^{\text{neighbors}} = \frac{N_Z}{N_S - 1}, \tag{3.5}$$

where N_Z is the number of neighboring surface sites, and N_S is the total number of surface sites. In the mean-field approximation, A and B are assumed to be independent and randomly distributed over an infinitely large surface [141, p.112], hence, Eq. (3.4) becomes:

$$\frac{\mathrm{d}\langle \mathrm{A} \rangle}{\mathrm{d}t} = -k \frac{N_Z}{N_S - 1} \left(\langle \mathrm{A} \rangle \langle \mathrm{B} \rangle + \Big\langle (\mathrm{A} - \langle \mathrm{A} \rangle)(\mathrm{B} - \langle \mathrm{B} \rangle) \Big\rangle \right). \tag{3.6}$$

If the surface is infinitely large, and the variables are independent, $N_S - 1 \approx N_S$ and the covariance is zero, *i.e.*,

$$\frac{\mathrm{d}\langle \mathrm{A} \rangle}{\mathrm{d}t} = -k \frac{N_Z}{N_S} \langle \mathrm{A} \rangle \langle \mathrm{B} \rangle. \tag{3.7}$$

By dividing both sides with N_S, the mean-field expression for the elementary reaction $\mathrm{A} + \mathrm{B} \longrightarrow \mathrm{AB}$ is:

$$\frac{\mathrm{d}\theta_{\mathrm{A}}}{\mathrm{d}t} = -k N_Z \theta_{\mathrm{A}} \theta_{\mathrm{B}}. \tag{3.8}$$

The coverage of X, θ_{X}, is defined as $\langle \mathrm{X} \rangle / N_S$, and is hence, an expectation value. The expression obtained in Eq. (3.8) is, in the mean-field approach, general for any intermediate and elementary reaction [146], *i.e.*, the time-derivative of the coverage of adsorbate X is

$$\frac{\mathrm{d}\theta_{\mathrm{X}}}{\mathrm{d}t} = \sum_i I_i^{\mathrm{X}} N_Z k_i g_i(\theta_1, ..., \theta_N). \tag{3.9}$$

Here, the summation runs over all elementary reactions involving the species X, I_i^{X} is the change of the number of X upon the elementary reaction, N_Z is the number of neighboring surface sites, k_i is the elementary reaction rate constant, and g_i is a function of the coverages. The coverages can, hence, be obtained from solving a set of coupled differential equations. In simple cases, or if assumptions are made about the reaction, analytical solution can be found [8, p.61]. The mean-field approach is often used to see trends between catalytic materials, and has been employed to elucidate the performance of catalytic materials in a range of different reactions [36–41]. However, to model reactions over alloys and nanoparticles, with a range of different sites, and to properly capture adsorbate-adsorbate interactions, other methods must be employed.

3.3 Kinetic Monte Carlo modeling

Kinetic Monte Carlo is a stochastic approach to propagate a chemical system along paths in the configurational space, satisfying the probability distributions of the chemical master equation [46, 147]. The simulations are coarse-grained, so that molecular vibrations are not explicitly considered, and only stable intermediate configurations are considered. Kinetic Monte Carlo has been employed to elucidate the catalytic properties in a range of different reactions where non-uniform structures or when adsorbate-adsorbate interactions give rise to altered kinetics [47–51]. Different kinetic Monte Carlo approaches exist with respect to how the stochastic propagation is performed, *e.g.*, the variable step size method, the random selection method, and the first reaction method [141]. In this work, a first reaction method approach has been employed [148] in accordance with the flowchart presented in Figure 3.2.

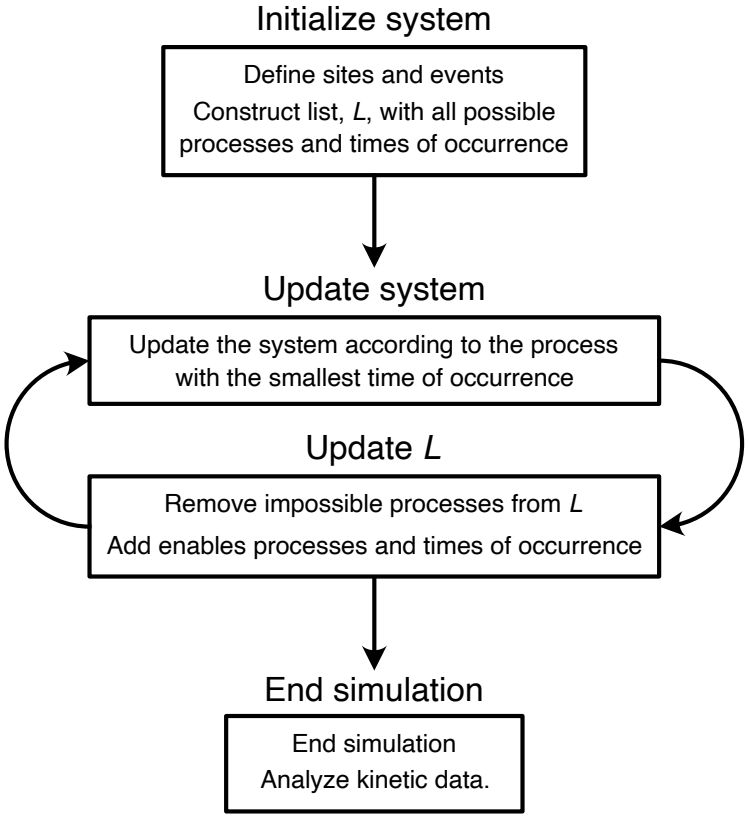

Figure 3.2: A flowchart of kinetic Monte Carlo simulations performed according to the first reaction method.

1. The system is initialized

- The kinetic Monte Carlo simulation is initialized according to the geometry of interest, *e.g.*, a (111) surface, a stepped surface, or a nanoparticle of certain shape and size.
- The catalytic sites are defined based on the geometry of the system. The sites may differ in character, depending on the chemical element and atomic coordination. The sites are connected to their neighboring sites, as to know whether events occurring over multiple neighboring sites are possible.
- All elementary reactions are defined, including criteria to determine whether they are possible given the state of the system. The potential energy landscapes for the different catalytic sites are described.
- The reaction conditions, such as temperature, partial pressures, and initial surface coverages are specified. The time of the simulation is set to the initial time.
- A list L is constructed, containing all initially possible transitions. In the case of an event occurring over two sites, each entry is specified by four variables: the specific elementary reaction, the two different sites, and the time of occurrence, defined as

$$t_{\text{occurrence}} = t - \frac{\ln u}{k}, \tag{3.10}$$

  where t is the current simulation time, u is a random uniform number in the interval (0,1], and k is the rate constant for the elementary reaction.

2. The system is propagated in time (repeatedly)

- The system is updated according to the event with the lowest time of occurrence, *i.e.*, t is set to $t^{\text{min}}_{\text{occurrence}}$, and the occupations of the sites are updated according to the event.
- Events that are disabled are removed from L. Events that are enabled due to the update are added to L with their associated times of occurrence. Events for which the rate constant has been altered due to *e.g.*, different adsorbate-adsorbate interactions are given new times of occurrences.
- In principle, it is also possible to update the reaction conditions, such as temperature and partial pressures. However, new times of occurrences must in these cases be calculated for each possible event.

3. The simulation is finalized

- The time evolution of the system is stopped if a certain simulation time is reached, or enough data has been collected.

3.3.1 Statistical averages from the first reaction method

The first reaction method should explore the configurational space stochastically, while resulting in the correct statistical averages. To show that this approach results in the correct average reaction times, consider an event M, with the corresponding rate constant k. As the time of occurrence is sampled from Eq. (3.10), it follows that

$$t' = t^{\min}_{\text{occurrence}} - t = -\frac{1}{k}\ln u = -\frac{1}{k}\ln(1-u) = F(u) \tag{3.11}$$

$$p(t') = \frac{\mathrm{d}}{\mathrm{d}t'}F^{-1}(t') = \frac{\mathrm{d}}{\mathrm{d}t'}\left(1-\mathrm{e}^{-kt'}\right) = k\mathrm{e}^{-kt'}, \tag{3.12}$$

where F^{-1} is the inverse function of F. The expectation value for the time of which the process occurs is therefore

$$\int_0^\infty t'\, k_j \mathrm{e}^{-k_j t'}\,\mathrm{d}t' = \frac{1}{k_j}. \tag{3.13}$$

Furthermore, if multiple processes $M_1, ..., M_N$ are possible with the corresponding rate constants $k_1, ..., k_N$, each process should occur with a probability proportional to its rate constant. The probability of process M_j occurring before any other process is obtained from Eq. (3.12) as

$$\begin{aligned} p(M_j) &= \int_0^\infty k_j \mathrm{e}^{-k_j t'_j}\left(\int_{t'_j}^\infty k_1 \mathrm{e}^{-k_1 t'_1}\mathrm{d}t'_1 \cdots \int_{t'_j}^\infty k_N \mathrm{e}^{-k_N t'_N}\mathrm{d}t'_N\right)\mathrm{d}t'_j = \\ &= \int_0^\infty k_j \mathrm{e}^{-t'_j\sum_{i=1}^N k_i}\,\mathrm{d}t'_j = \frac{k_j}{\sum_{i=1}^N k_i}. \end{aligned} \tag{3.14}$$

Hence, both the reaction times and the probability of processes occurring result in correct statistical averages.

3.4 Comparison between mean-field and kinetic Monte Carlo modeling

In the simple case of adsorption and desorption of A, where each A occupies a single site and no adsorbate-adsorbate interactions are present, it is possible to derive an

exact analytical expression for the coverage. Starting from an empty surface, Eq. (3.9) results in

$$\frac{\mathrm{d}\theta_{\mathrm{A}}(t)}{\mathrm{d}t} = k_{\mathrm{ads}}\theta_*(t) - k_{\mathrm{des}}\theta_{\mathrm{A}}(t) \implies \theta_{\mathrm{A}}(t) = \frac{K}{K+1}\left(1 - \mathrm{e}^{-(k_{\mathrm{ads}}+k_{\mathrm{des}})t}\right), \quad (3.15)$$

where the equilibrium constant $K = k_{\mathrm{ads}}/k_{\mathrm{des}}$. Here, the partial pressure of A has been included in the adsorption rate constant. Hence, the equilibrium constant does in this case depend on both temperature and partial pressure. In Figure 3.3, the analytic solution of the time-evolution of the coverage is presented with a dashed black line. When the coverage is lower than the equilibrium coverage, the adsorption rate dominates. Over time, the equilibrium coverage is reached, and the adsorption and desorption rates are equal. Kinetic Monte Carlo simulations of the adsorption and desorption of A on a (10×10)-grid and a (100×100)-grid are presented with red and blue lines, respectively.

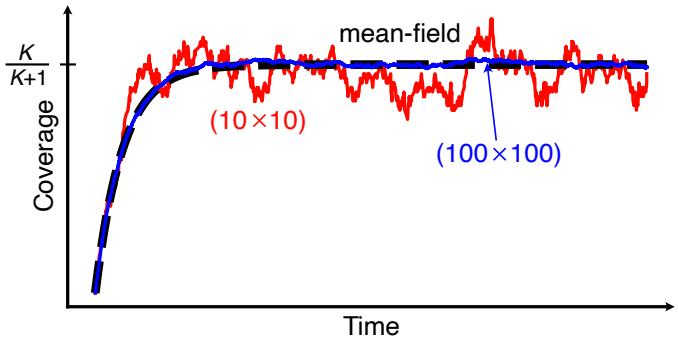

Figure 3.3: The kinetic Monte Carlo-simulated occupations on the surface as a function of time, for a (10×10)-grid (red) and a (100×100)-grid (blue), compared with the analytical expression of the coverage (black).

For the (100×100)-grid, the deviations from the analytical solution are small, as the coverage is merely an average of a large number of sites. The (10×10)-grid can be interpreted as describing the local coverage for a smaller region of the (100×100)-grid. Here, the surface coverage fluctuates significantly. For large grids, or a large number of simulations, the expectation value of the surface occupation will converge to the average coverage. However, it should be emphasized that local fluctuations are still present. For nano-sized catalysts, the (10×10)-grid may represent the entire catalyst. The analytical expression could, in this case, not capture the oscillating behavior of the total coverage. This could have significant consequences for the description of catalytic reactions, as the reaction rate constant is sensitive to changes in local environment. Furthermore, if a reaction only

occurs at high coverages, the reaction rate would in the mean-field approximation be constant and low. However, if fluctuations are captured, the reaction rate may momentaneously be high, resulting in average reaction rates greater than those obtained from the mean-field approximation. In conclusion, the expectation values are in the kinetic Monte Carlo simulations obtained from averaging a large number of data points, while maintaining the atomic description. This is in contrast to the mean-field approximation, where the averaging is part of the formalism, neglecting the site-resolution. In this simple case, the coverages will converge towards the same values. However, this is generally not the case. For diatomic dissociative adsorption, without desorption or diffusion, the mean-field approximation would result in a completely covered surface. This might not be the case if the system is modeled with site-resolution, as two neighboring surface sites are required for the adsorption.

As the mean-field approximation assumes independent adsorbates, it can not accurately capture adsorbate-adsorbate interactions. It is, however, possible to mimic the effects of the interactions, to obtain more reasonable coverages and reaction rates. The adsorbate-adsorbate interactions could in the mean-field approach be incorporated by scaling of the adsorption energies as a function of total coverage [149, 150]. Kinetic Monte Carlo simulations, on the other hand, provide a site-specific description of the intermediate occupations. The adsorption-adsorption interactions can therefore be explicitly described as functions of the local environment [151–153]. In Figure 3.4, the effects of adsorbate-adsorbate interactions for the single-site-adsorption and desorption of A on a $(24 \times 12\sqrt{3})$rect.(111) surface is visualized.

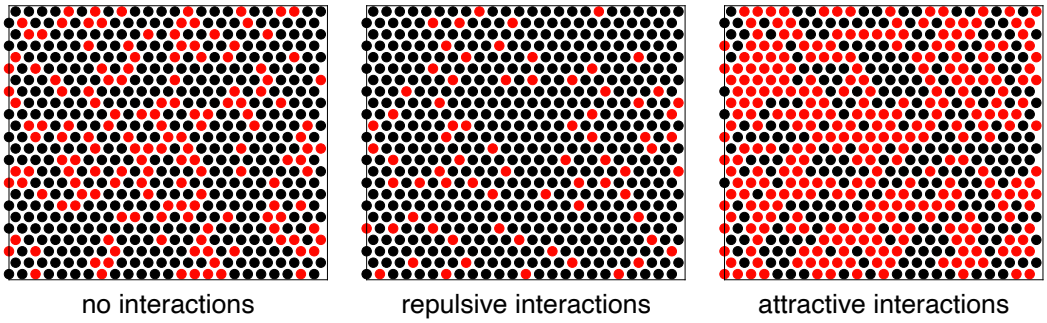

Figure 3.4: The coverage after 100000 adsorption/desorption events for different adsorption-adsorption interactions.

In the left figure, no adsorption-adsorption interactions are included. The adsorp-

tion energy is slightly endergonic ($\Delta G_{\text{ads}} > 0 \implies K < 1$), so that the time-averaged coverage is below 0.5. The adsorbates are randomly distributed on the surface. In the middle figure, a pair-wise repulsive interaction between neighboring adsorbates is included. The probability of adsorbates residing in neighboring sites is therefore reduced, which results in a lower equilibrium coverage. In the right figure, a pair-wise attractive interaction between neighboring adsorbates is included. The adsorption is, hence, stabilized next to another adsorbate, and islands of adsorbates are formed, resulting in a higher equilibrium coverage. The site-specific description could have significant consequences for the description of catalytic reactions. As mentioned previously, the reaction rate constants could be affected by neighboring species on the surface. Furthermore, the possibility of elementary reactions occurring relies on neighboring surface species, which is altered due to *e.g.*, the formation of islands. Local knowledge of the occupations can, thus, provide a more accurate description of catalytic reactions.

3.5 Analysis of reaction kinetics

By having site-specific information of the processes on the surface, it is possible to elucidate main reaction pathways, potential kinetic bottlenecks, and the effects of local coverages, which could aid in optimizing the performance of the catalyst. To describe the efficiency of a catalyst under specific reaction conditions, turn-over frequency (TOF) is commonly used. The TOF describes the number of products formed per site every second. The TOF should preferably be high for the desired products and low for the by-products formed in side-reactions. A way to measure the distribution of the products is the selectivity. The selectivity S towards a product p is

$$S_p = \frac{\text{TOF}_p}{\sum_i \text{TOF}_i}, \tag{3.16}$$

where the summation is performed over all products. For certain reactions, it is challenging to find a catalyst and reaction conditions that obtain a high TOF towards the desired product, while also maintaining a high selectivity. An example is the direct formation of H_2O_2 from H_2 and O_2. An efficient catalyst should bind O_2 strongly enough to facilitate the reaction towards H_2O_2. However, if O_2 is bound too strongly, the selectivity will be reduced due to irreversible O–O bond breaking, resulting in the formation of H_2O [80].

Reaction orders and apparent activation energies are ways to to describe the efficiency of a catalyst, as a function of reaction conditions. These could be used to optimize the reaction conditions. The analysis is in this case performed via the

phenomenological rate expression towards a product p:

$$r_p^+ = C_p \mathrm{e}^{-E_p^{\mathrm{app}}/k_\mathrm{B}T} \prod_i [\mathrm{X}_i]^{n_{i,p}}, \tag{3.17}$$

where C is the pre-factor, E^{app} is the apparent activation energy, [X] is the activity of species X, and n is the reaction order. The activity is often approximated as the partial pressure of a gas or the concentration of a solvated species [8, p.29]. The reaction order $n_{i,p}$ for any reactant, and the apparent activation energy E_{app} towards a product p is obtained from Eq. (3.17) as [8, p.25–38]:

$$n_{i,p} = [\mathrm{X}_i] \frac{\partial \ln r_p^+}{\partial [\mathrm{X}_i]} \tag{3.18}$$

$$E_p^{\mathrm{app}} = k_\mathrm{B} T^2 \frac{\partial \ln r_p^+}{\partial T}. \tag{3.19}$$

Here, the pre-factor, apparent activation energy, the activities and the reaction orders are all assumed to be independent of temperature. This is, however, not the case, and their values will therefore depend on the specific reaction conditions. As reaction orders and activation energies can be measured experimentally, the concepts act as a bridge between computational models and experiments.

4

Charge transfer in catalytic reactions

Operational catalysts are multi-component systems, often constituted of metals in contact with oxides and liquid solvents. A catalytic reaction is, thus, not restricted to occur on one part of the catalyst. In some cases, the catalytic activity is improved, by a separation of the reaction, in which elementary reactions occur on different parts of the catalyst [154]. Moreover, the presence of several different constituents results in interface regions between the components. The interfaces could modify the properties of the components, as compared to the isolated materials. The modification can have different origin. For example, the lattice mismatch can induce strain in the materials. The interfaces could also lead to polarization in the materials, and in some cases, electron transfer between the components. These modifications are sometimes referred to as materials synergy. Adsorbates on the surface can further induce the synergetic interplay between the catalyst components, affecting the kinetics of the reaction. Identifying the underlying reasons for experimentally observed synergies is often difficult. To aid in the understanding of the synergies, model systems with a reduced structural complexity is valuable, in which the interplay between different catalyst constituents could be isolated.

In this chapter, the interplay between metal catalyst surfaces and an aqueous solution is discussed. In particular, the charge transfer processes occurring at the metal/water interface for adsorbed H_2 are described, and its kinetic implications for the direct formation of H_2O_2 from H_2 and O_2 is discussed. The adsorption of H_2 is further employed to elucidate the interplay between metal nanoparticles and oxide supports, and its possible kinetic implications for the hydrogenation of CO_2 to methanol.

4.1 Charge transfer at the metal/water interface during H_2O_2 synthesis

It is well-known that a liquid solution can have significant consequences for the activity and selectivity of a catalytic reaction [6, 10]. The altered kinetics could have different origin, such as the solvation of intermediates and transition states on the surface [155, 156], or competitive adsorption of solvent molecules on the catalyst surface. In hydrogenation reactions, methanol from the solution has been proposed to adsorb on the surface, forming ligands that co-catalyze the reaction by transferring hydrogen between intermediates [157, 158]. A similar mechanism could occur in water solutions, were water molecules act as a bridge in a proton-coupled electron transfer [90, 158].

Another mechanism that has been proposed to occur at the metal/water interface is the complete charge separation of hydrogen [79, 159–161]. In this process, H is separated into a proton solvated in the solution, and an electron delocalized in the metal surface. Results from *ab initio* molecular dynamics simulations of the charge separation of H at the metal/water interface is presented in Figure 4.1. Initially, H is adsorbed on the metal surface below a water solution (left). The transition state is reached when H diffuses on top of a metal atom, below a water molecule (middle figure). In the final configuration (right), a hydronium ion (H_3O^+) has been formed, which is solvated in the water solution over a negatively charged metal surface.

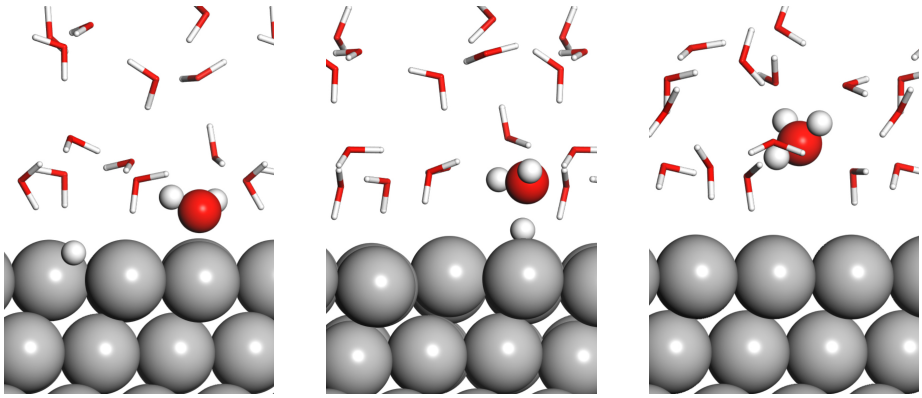

Figure 4.1: Atomic structures of the charge separation process at the interface between Pt(111) and a water solution. The initial (left) and final (right) configurations are optimized structures, from molecular dynamics simulations, whereas the transition state configuration is taken from a constrained molecular dynamics simulation. Atomic color codes: Pt (gray), O (red), and H (white).

The influence of a metal/water interface, and the charge separation of H, in the direct formation of H_2O_2 from H_2 and O_2 over dilute PdAu nanoparticles in a water solution, is investigated in **Paper I**. The changes in free energy for the charge separation of H at the Au(111)/water interface is shown in Figure 4.2. The free energy gradients for the charge separation are calculated with constrained molecular dynamics simulations for different H$-$H$_2$O distances, and the free energy profile is obtained from thermodynamic integration. H is initially adsorbed on the Au surface. The transition state is reached when H diffuses on top of an Au atom, directly below H_2O. In the final configuration, an H_3O^+ ion is formed, and the electron is delocalized in the Au surface. The charge separated state is stable, and the process is associated with a low free energy barrier of 0.28 eV. To explore the generality of the effects owing to the metal/water interface, the charge transfer processes are explored also for the (111)-surfaces of Cu, Ag, Pd, and Pt, in **Paper II**. It is found that the charge separation is facile and exothermic, or close to thermo-neutral, also at the interfaces between Ag, Pd, and Pt and water. For Cu, however, the charge separation has a high free energy barrier of 0.85 eV. Moreover, the presence of water is found to stabilize the adsorption of O_2, as a result of a metal-to-O_2 charge transfer, increasing the strength of the hydrogen bonds between O_2 and water.

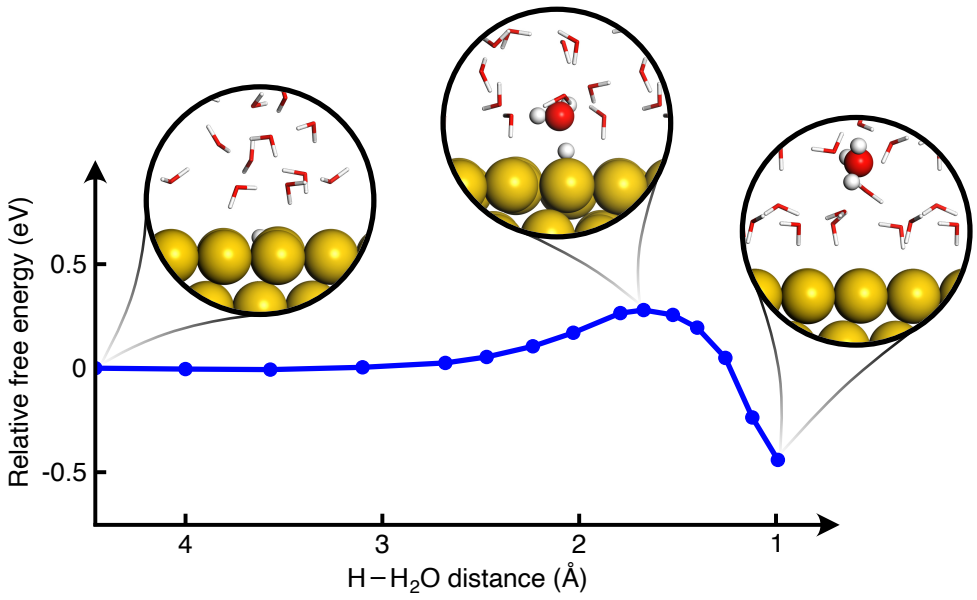

Figure 4.2: Relative free energies for the charge separation of H at the Au(111)/water interface. Atomic visualizations for three different H-H_2O distances are included, corresponding to the initial, transition and final states. Atomic color codes: Au (yellow), O (red), and H (white).

4.1.1 Energy deconvolution of the charge separation

The different energy contributions in the charge separation of H can be analyzed to rationalize the stable state of a water-solvated proton over a negatively charged metal surface. A schematic visualization of the energy contributions is presented in Figure 4.3.

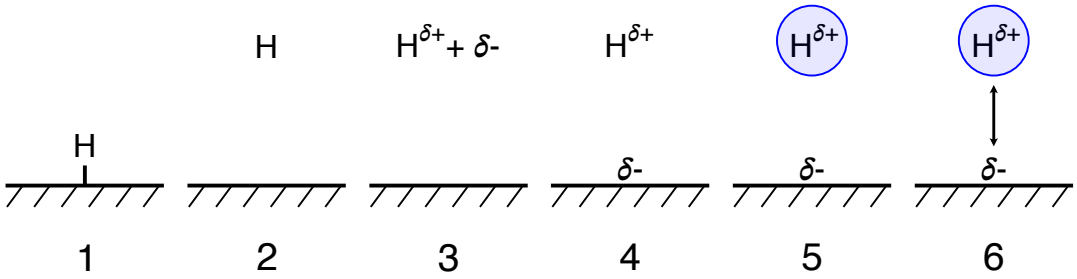

Figure 4.3: A schematic visualization of the different energy contributions in the charge separation of H at the metal/water interface.

The contributions are:

$1 \rightarrow 2$ – Desorption of H from the metal surface.

$2 \rightarrow 3$ – Ionization of H.

$3 \rightarrow 4$ – Electron transfer to the metal surface.

$4 \rightarrow 5$ – Solvation of the proton.

$5 \rightarrow 6$ – Coulomb interactions between the proton and the metal surface.

Of the different contributions, processes $(1 \rightarrow 2)$ and $(3 \rightarrow 4)$ are significantly metal dependent. The desorption energy of H from the surface depends on the metal-H binding strength, whereas the electron transfer energy contribution is proportional to the metal work function. In this case, the presence of water can decrease the work function as compared to vacuum conditions [162]. The charge separation is favored by surfaces with weak H_2 adsorption energies and high work functions. However, the facility of the process depends on the possibility of H_2 adsorption and dissociation on the surface. Hence, while Au(111) has a high work function [163], and binds H weakly, alloying with an active metal, such as Pd, is necessary to facilitate the dissociation of H_2.

4.1.2 Kinetic implications of the charge separation of H

The charge separation of H at the metal/water interface can have significant implications for the kinetics of hydrogenation reactions. Whereas interactions between adsorbates and the solution shift the energies in the reactions, the charge separation of H enables new reaction pathways in the reaction. The consequences of the charge separation on the potential energy surface are visualized in Figure 4.4.

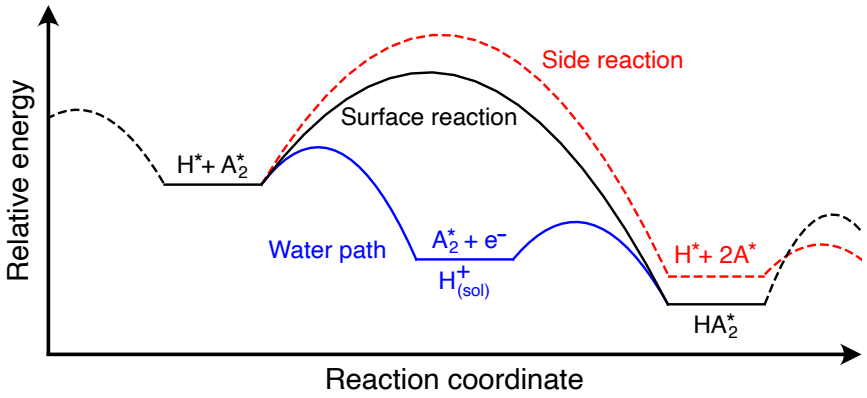

Figure 4.4: A partial potential energy surface highlighting the implications of the charge separation process at the metal/water interface. * denotes an intermediate bound to the surface. On the metal surface, the reaction towards the desired product (black) is competing with the formation of a by-product (red). The charge separation of H enables an alternative reaction pathway in the catalytic reaction (blue).

In the reaction (Figure 4.4), H should react with A_2, forming HA_2 (black). The formation of HA_2 is on the catalyst surface competing with the undesirable A – A bond breaking, forming 2A (red). The relative heights of the energy barriers between the two paths give some insight into the selectivity of the reaction. However, it should be noted that the rate of the side reaction can be greater than the formation of HA_2 at a low H coverage. If charge separation of H is preferred, an alternative reaction path is enabled (blue). After the charge separation, the proton recombines with the electron at A_2, forming HA_2. Low barriers for the charge transfer processes are beneficial in the formation of HA_2. A too stable charge separated state is not desirable, as the decomposition of HA_2 into $A_2 + e^- + H^*_{sol}$ becomes favorable, which would decrease the activity and selectivity in the reaction. It should be noted that the stable charge separated state results in a negatively charged metal surface during reaction. The consequences of this are discussed in Section 4.2.2.

A_2 in Figure 4.4 denotes a general intermediate. In the direct formation of H_2O_2 from H_2 and O_2, the formation of OOH and H_2O_2 are directly competing with the

undesirable O – O bond breaking in adsorbed O_2, OOH, and H_2O_2, resulting in the formation of water [80, 85, 164]. Single-atom alloy PdAu nanoparticles, solvated in a water solution has experimentally been shown to obtain H_2O_2 selectivities close to 100 % [90]. In **Paper I**, the mechanism of the direct formation of H_2O_2 from H_2 and O_2 over dilute PdAu nanoparticles in a water solution is investigated. It is found that Pd monomers in the surface of the nanoparticles enable the dissociation of H_2, after which, a proton is desorbed to the water solution and an electron is donated to the nanoparticle surface. The proton and electron recombine at O_2 species adsorbed on Au atoms at edges and corners of the nanoparticles. The facile charge separation of H, and the high energy barriers for O – O bond breaking on Au sites, enable the possibility to obtain high selectivities towards H_2O_2 over dilute PdAu catalysts. The presented reaction mechanism, in which the elementary reactions are separated over different sites, has later been experimentally confirmed for the reaction over Pt_1Au catalysts [165].

4.2 Charge transfer at the metal/oxide interface during methanol synthesis

The synergy between different catalyst constituents can have significant consequences for reactions catalyzed by metal nanoparticles supported on an oxide support [166, 167]. The synergy and improved catalytic performance is often assigned to the altered chemical properties at the metal/oxide interface [168, 169]. However, the effects of the support may reach further than the interface sites. The support could, for example, induce strain in the metal particles [170], hence influencing the potential energy surface [34]. In some cases, the reaction is separated, so that some elementary reactions occur on the metal nanoparticles, whereas other processes occur on the support [171]. Another type of metal/oxide synergy is the transfer of charge between oxide supports and metal nanoparticles, or thin oxide films supported on a metal surface [172]. The transfer of charge between the oxide and the metal has been shown to be promoted by the adsorption of molecules on the oxide [173–175]. For example, the adsorption energy of H_2 on thin oxide films supported on a metal is significantly increased as compared to the adsorption on a bare oxide surface, owing to an oxide-to-metal electron transfer [176, 177].

H_2 can adsorb in two different configurations on oxide surfaces [176]. The two adsorption configurations are shown in Figure 4.5, for the case of Wurtzite ZnO($10\bar{1}0$). The heterolytic adsorption (left) results in the formation of one oxygen–proton bond, and one metal–hydride bond. This adsorption configuration is charge neutral and associated with an adsorption energy of -0.05 eV (exothermic). The homolytic

adsorption (right), results in the formation of two oxygen–proton bonds. This adsorption is not charge neutral with respect to H, and results in two excess electrons that delocalize and reside in the oxide conduction band. The homolytic adsorption is therefore unfavorable, being 0.34 eV (endothermic). Previous findings have shown that the heterolytic adsorption is preferred on oxides such as MgO [178], ZnO [179, 180], and ZrO_2 [181]. However, for surfaces where the oxidation state of the metal cations can change, excess electrons, instead of delocalizing in the conduction band, reduce the metal cations. Therefore, the homolytic adsorption is more stable on *e.g.*, CeO_2, for which the oxidation state of Ce can change from Ce^{4+} to Ce^{3+} [182, 183].

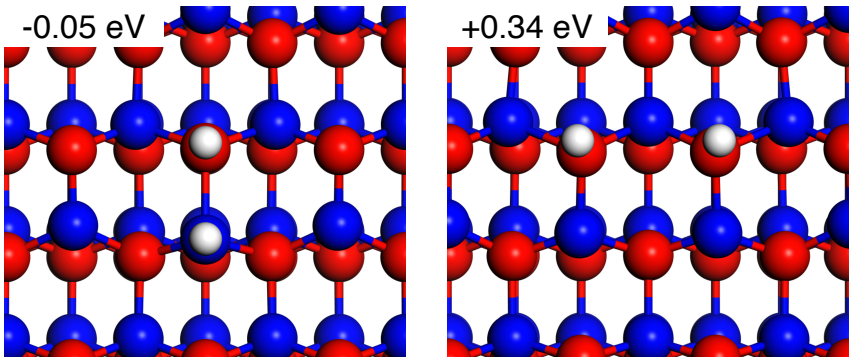

Figure 4.5: Optimized structures of the heterolytic (left) and homolytic (right) adsorption of H_2 on ZnO($10\bar{1}0$) with the corresponding adsorption energies. Atomic color codes: Zn (blue), O (red), and H (white).

The unstable homolytic adsorption of H_2 is a consequence of the low stability of the excess electrons. However, in prototypical catalysts, oxide surfaces are often in direct contact with metal nanoparticles. The metal can, in these cases, act as a reservoir for the electrons, hence, stabilizing the homolytic adsorption of H_2. The influence of a supported nanoparticle on the adsorption of H_2 is explored in **Paper IV** and **Paper V**. In Figure 4.6, the two adsorption configurations of H_2 are shown for the case of a ZnO($10\bar{1}0$) surface with a supported Pt nanoparticle. The heterolytic adsorption configuration (left) is slightly destabilized by the presence of a Pt nanoparticle, being 0.06 eV (-0.05 eV in the absence of a Pt nanoparticle). However, the homolytic adsorption of H_2 (right) is significantly stabilized to -1.91 eV (0.34 eV in the absence of a Pt nanoparticle). The stabilization of homolytically adsorbed H_2 is a result of the excess electrons transferring to the Pt nanoparticle. The charge transfer and stabilization of homolytically adsorbed H_2 in the presence of a supported metal nanoparticle are found to be general for different metals, oxides and oxide surface orientations.

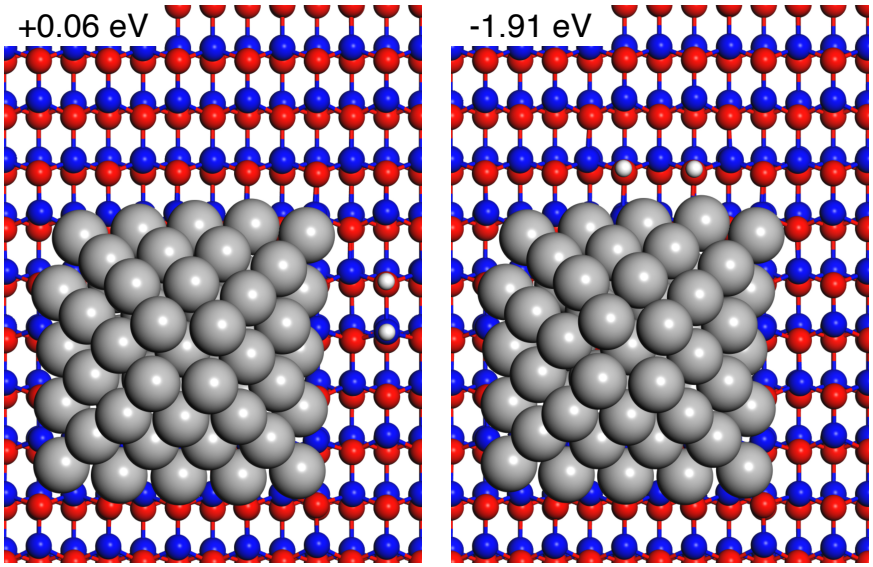

Figure 4.6: The heterolytic (left) and homolytic (right) adsorption configurations of H_2 on ZnO($10\bar{1}0$) close to a supported Pt nanoparticle. Atomic color codes: Pt (gray), Zn (blue), O (red), and H (white). Note that the homolytic adsorption of H_2 is significantly stabilized as compared to the adsorption in the absence of a Pt nanoparticle.

4.2.1 Energy contributions in homolytic H_2 adsorption

A schematic visualization of the different energy contributions in the adsorption of $\frac{1}{2}H_2$ on an oxygen ion in the oxide surface is presented in Figure 4.7.

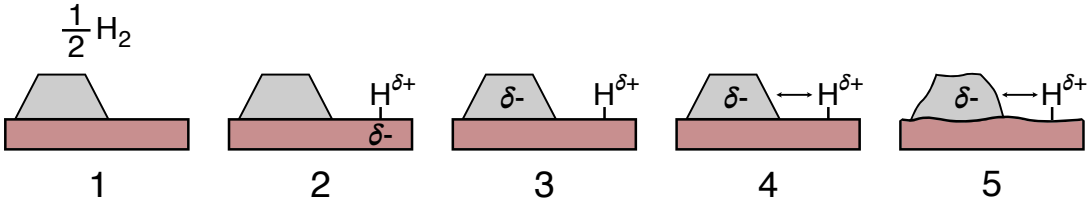

Figure 4.7: A schematic visualization of the different energy contributions in the homolytic adsorption of $\frac{1}{2}H_2$ on the oxide in the presence of a metal nanoparticle.

The contributions are:

$1 \rightarrow 2$ – Formation of an O^{2-}–H^{+} bond (and scission of H–H bond).

$2 \rightarrow 3$ – Oxide-to-metal electron transfer.

$3 \rightarrow 4$ – Coulomb interactions between the negatively charged metal and H^{+}.

$4 \rightarrow 5$ – Distortions to the metal nanoparticle and oxide surface [174].

The reason for the oxide-to-metal charge transfer, and the associated energy contribution, can be rationalized and estimated from the density of states (DOS). In Figure 4.8, schematic DOSes for an oxide surface (left), and for an oxide surface with a supported metal nanoparticle (right) are visualized. The electronic states corresponding to the oxide and the metal nanoparticle are shown in red and black, respectively. The Fermi energies are marked with dashed gray lines. For a homolytic adsorption of H_2 on the bare oxide surface, the excess electrons occupy states in the conduction band. However, when a metal nanoparticle is present, electronic states around the Fermi energy are available. A transfer of the excess electrons from the oxide conduction band, to the unoccupied metal states, is associated with a lower electronic energy, and hence, a stabilization of the homolytic adsorption of H_2.

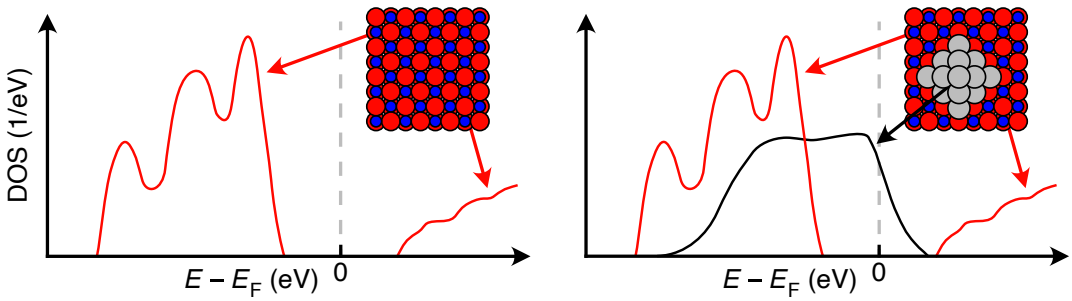

Figure 4.8: A schematic visualization of the density of states for an oxide surface (left) and an oxide surface with a supported metal nanoparticle (right). The oxide states are shown in red, whereas the metal states are presented in black. Atomic color codes: metal [NP] (gray), oxide cation (blue), and oxygen (red).

The lower energy states of the metal as compared to the conduction band of the oxide (Figure 4.8) can also explain charge transfer phenomena occurring in other processes where excess electrons are present. One example is the formation of an

oxygen vacancy in the oxide surface, which generates two excess electrons. On the bare oxide surface, the formation of oxygen vacancies results in occupied electronic states in the band gap [184]. In **Paper VI**, oxygen vacancy stabilities in the presence of a supported metal nanoparticle are investigated. For vacancies formed close to a metal nanoparticle, no new electronic states are formed in the oxide band gap. The electrons are, instead, transferred to the metal nanoparticle, and the oxygen vacancy is stabilized.

4.2.2 Kinetic implications of oxide-to-metal charge transfer

The charge separation of H at the metal/water interface and the homolytic adsorption of H_2 at the metal/oxide interface results in a stabilization of H in the water solution and on the oxide, respectively. H may in these cases interact with adsorbed species on the metal phase, or act as a hydrogen buffer in hydrogenation reactions. Furthermore, the charge transfer results in negatively charged metal surfaces and nanoparticles under reaction conditions. The possible implications of the charge transfer for an elementary reaction AB $\longrightarrow$ A + B are visualized in Figure 4.9. The intermediate stabilities and energy barrier on a neutral metal are presented in black. On the negatively charged metal (blue), the intermediate stabilities and energy barrier may be altered.

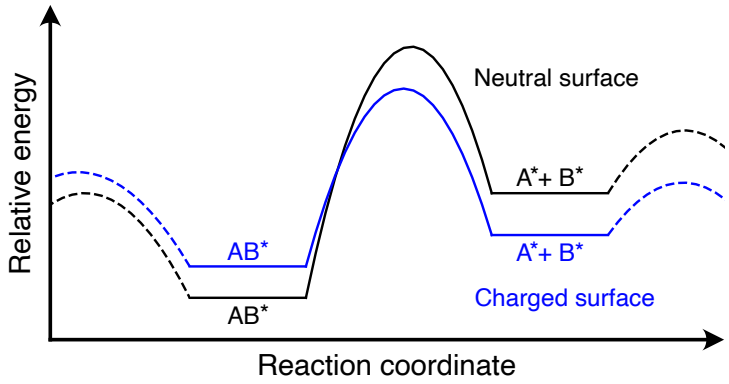

Figure 4.9: A partial potential energy surface highlighting possible implications of charge transfer to the metal surface under reaction conditions. The energies on a neutral metal are presented in black and the energies of the intermediates on a negatively charged metal are presented in blue.

The implications of oxide-to-metal charge transfer in the hydrogenation of CO_2 to methanol over Cu nanoparticles supported on ZnO is investigated in **Paper IV**.

In the reaction, the energy barrier for the scission of the C−O bond in adsorbed formic acid is found to be sensitive to the charge state of Cu. The charge transfer, due to homolytically adsorbed H_2 on the ZnO support, reduces the energy barrier for the C−O bond scission by ∼0.1 eV, which corresponds to a factor ∼10 increase in elementary reaction rate at operational temperatures.

5

Reaction kinetics over nanoparticles

Kinetic modeling relies on an accurate description of the potential energy surface. This is commonly realized from calculations for adsorption and transitions state configurations on extended model surfaces. These energies can be employed directly to describe the kinetics over single crystal catalysts, with one type of catalytic site. Industrially, however, metal nanoparticles are the preferred catalyst, owing to the large surface-to-volume ratio. For larger nanoparticles, most of the surface resembles extended surfaces. For smaller nanoparticles, the surface is constituted of a large fraction of low-coordinated metal atoms at the edges and corners, associated with significantly altered catalytic properties. The configuration space of catalytic sites, adsorbates, and adsorbate-adsorbate interactions is in this case large, and explicit calculations for each possible configuration is unfeasible, and approximations are needed.

As the chemical properties of the different metal atoms in a nanoparticle are correlated, it is often possible to find descriptors to describe the catalytic properties. This is known as scaling relations. Whereas scaling relations enable an approximate description of the entire potential energy surface, the existence of relations is one reasons why the optimization of metal catalysts is difficult. The mere existence of scaling relations stresses the limitation of the possible property space for materials.

In this chapter, trends between local coordination of catalytic sites and the potential energy surface are reviewed. Kinetic implications of reactions occurring over different catalytic sites are discussed, and the reaction mechanism of direct formation of H_2O_2 from H_2 and O_2 in water-solvated, dilute PdAu nanoparticles

is described. This is followed by a discussion on the dynamic behavior of nanoparticles in inert and reactive atmospheres.

5.1 Descriptors and scaling relations

The stability of an intermediate on a metal surface depends on the electronic structure, and specifically the *d*-band center, of the adsorption site [24, 25, 31–34]. The *d*-band center shifts with the local environment of the metal atoms. Therefore, intermediate stability and elementary reaction energy barriers on a catalyst surface can also be described by the local coordination of the catalytic sites [185–187]. The coordination number, *i.e.*, the number of nearest neighbors, is one way to describe the local coordination. A refined descriptor, that also captures the effects of longer-ranged coordination, is the generalized coordination number (GCN) [188, 189]. The GCN of a catalytic site, i, is defined as

$$\mathrm{GCN}_i = \frac{1}{\mathrm{CN}_{\mathrm{max},i}} \sum_j \mathrm{CN}_j, \tag{5.1}$$

where $\mathrm{CN}_{\mathrm{max},i}$ is the maximum number of nearest neighbors for the specific site, and the summation is performed over all nearest neighbors. The catalytic site could be either one or more atoms. In an FCC crystal structure, the maximum number of nearest neighbors for a single atom is 12, whereas the maximum coordination number for a bridge site between two atoms is 18. By calculating the adsorption energies of intermediates on extended surfaces with different GCN, it is often possible to find linear relations between GCN and adsorption energies. The relation between a descriptor and the adsorption energies of intermediates are sketched in the left panel of Figure 5.1.

Often, it is also possible to find relations between the stability of intermediates in an elementary reaction, and energy barriers, schematically visualized in the middle panel of Figure 5.1. Here, f is a function specifying the degree of which each intermediate stability affects the energy barrier [35]. The scaling relations are an important tool to interpolate the potential energy surface calculated on extended model surfaces, to catalytic sites with other local coordination. By combining the relationships between the descriptors, adsorption energies, and the energy barriers, the reaction rate on a single active site often follow the, so-called, volcano curve presented in the right panel of Figure 5.1.

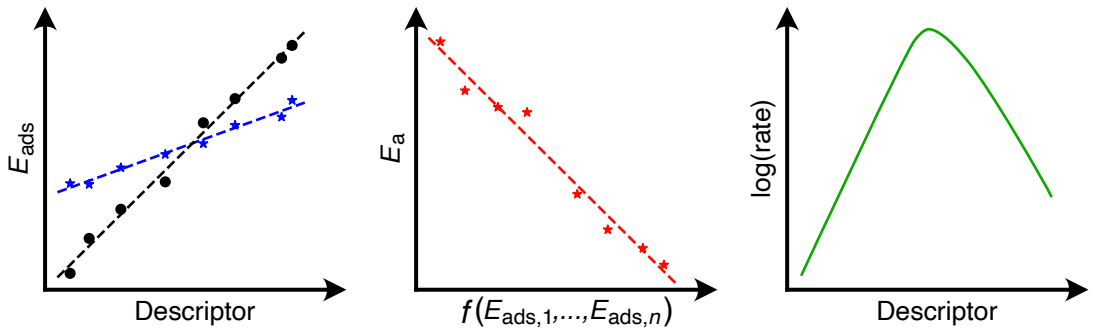

Figure 5.1: Scaling relations in the description of different catalytic sites. (Left) Relation between a descriptor and the adsorption energy of intermediates. (Middle) Relation between intermediate stabilities and energy barriers. (Right) The (log) rate of a reaction as a function of the descriptor.

5.2 Kinetic coupling in catalytic reactions

The descriptor value which maximizes the elementary reaction rates could differ between elementary reactions on the surface, *e.g.*, for some elementary reactions, a low coordination of the catalytic site is preferred, whereas for other processes, a high coordination could be beneficial. A separation of the reaction on different sites cannot occur on surfaces with only one type of site. However, it is possible on nanoparticles, where a large number of non-equivalent sites are present. The influence of a multitude of different sites in a catalytic reaction is visualized in Figure 5.2.

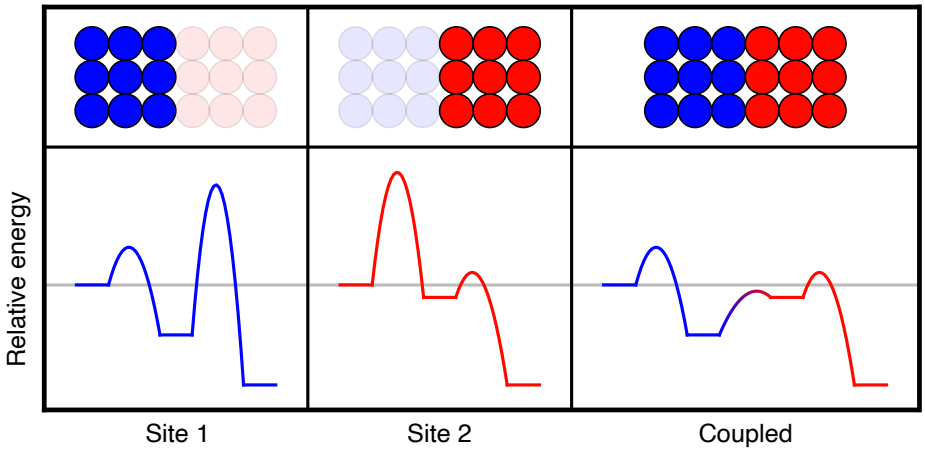

Figure 5.2: The potential energy surface of a reaction containing two elementary reaction steps for (left) an isolated site 1, (middle) an isolated site 2, and (right) a coupled system of site 1 and site 2.

If the reaction occurs solely on site 1, the first elementary reaction step is associated with a low barrier, whereas the second step has a high barrier. In this case, intermediates could overcome the first barrier, where after they are stuck, and the total reaction rate is low. The situation is reversed if only site 2 is present. In this case, the first barrier is high, and can not be overcome, resulting in a low reaction rate, despite the low second barrier. If the reaction is instead occurring over a system where both site 1 and site 2 are accessible, the situation is changed. After the first elementary reaction has occurred on site 1, the intermediates could, in the coupled system, diffuse to site 2 where the second reaction can occur, resulting in an increased reaction rate.

Due to the strong relations between differently coordinated sites and the chemical properties, it is difficult to find mono-metallic catalysts where the potential energy surfaces are as different as between site 1 and site 2 in Figure 5.2. Mixing two different metals, forming an alloy, could shift the binding energies of intermediates. However, the alloy typically preserves the linear relations between adsorption energies and energy barriers in elementary reactions [190]. One way of circumventing the linear scaling relations is to introduce metal monomers in the surface of another metal host, forming a single-atom alloy (SAA) [190–192]. SAAs of PdCu [57, 193], PdAg [194], and PdAu [69, 195] have been shown to be especially selective in hydrogenation reactions. In the case of direct H_2O_2 formation from H_2 and O_2 over dilute PdAu, selectivites close to 100% have been measured in water solutions [90].

5.3 Site communication in direct H_2O_2 synthesis

In **Paper I**, the direct formation of H_2O_2 from H_2 and O_2 is explored over SAA catalysts of Pd monomers dispersed in an Au host. The potential energy surface is mapped with density functional theory calculations over differently coordinated Pd monomers, taking the effects of the water solution into account. The potential energy surface over different Au sites is described by generalized coordination numbers. The kinetics of the reaction is simulated with kinetic Monte Carlo simulations. For Pd atoms residing in an extended Au(111) surface, all elementary reactions occur on the Pd atoms, and the selectivity towards H_2O_2 is high. The high selectivity towards H_2O_2 in the reaction over dilute PdAu nanoparticles is, however, not only a consequence of the high selectivity over Pd atoms residing in Au(111) facets. Whereas the Pd monomers are crucial for dissociating H_2 in the reaction, the main reaction path is H_2O_2 formation on low-coordinated Au sites at the nanoparticle edges and corners. The main reaction mechanism is presented in Figure 5.3.

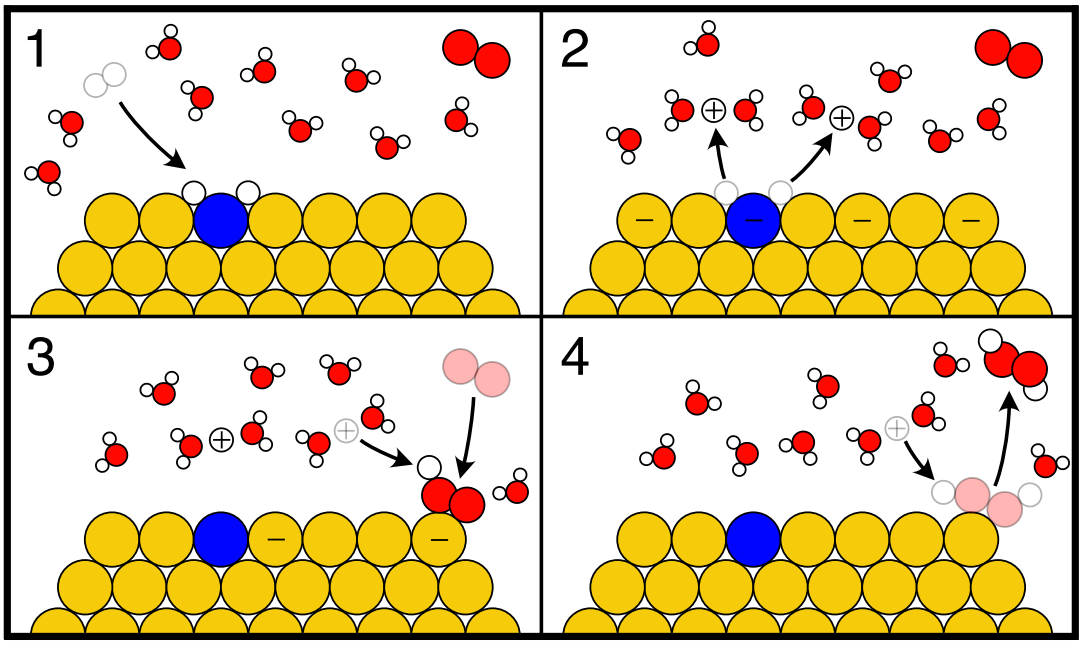

Figure 5.3: The mechanism in the direct formation of H_2O_2 from H_2 and O_2 over dilute PdAu nanoparticles in a water solution. Atomic color codes: Au (yellow), Pd (blue), O (red), and H (white).

The main reaction mechanism is:

(1) Dissociation of H_2 on Pd monomers in the surface.

(2) Charge separation of H, forming a stable intermediate state with protons solvated in the water solution, over a negatively charged metal surface.

(3) Adsorption of O_2 on low-coordinated Au sites, and the subsequent recombination of a proton and an electron, forming OOH.

(4) A second proton-electron recombination, forming H_2O_2, which is desorbed from the surface.

The separation of the reaction between Pd and Au, and hence the selectivity towards H_2O_2, is sensitive to the amount and placement of Pd monomers in the Au nanoparticle surface. In Figure 5.4, the selectivity towards H_2O_2, at H_2 and O_2 partial pressures of 1 bar and 286 K, for four different nanoparticle compositions are presented.

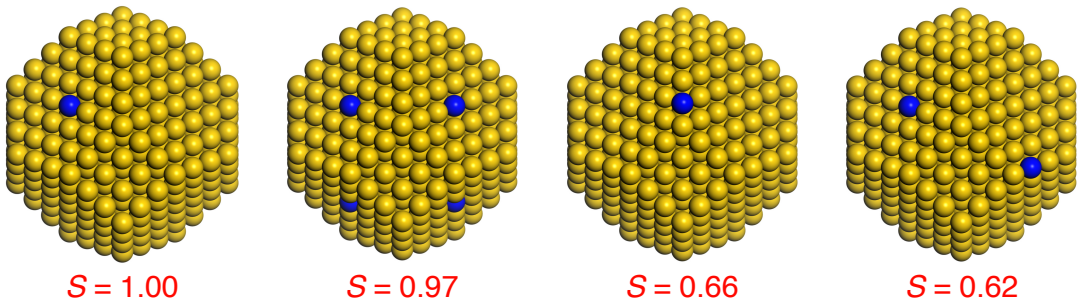

Figure 5.4: The selectivity (S) towards H_2O_2 for different compositions of Pd monomers in the Au nanoparticle surface. Atomic color codes: Au (yellow) and Pd (blue).

If a Pd monomer is located in the (111)-facet, the reaction is separated so that the formation of H_2O_2 succeeds on the Au sites. If more Pd monomers are placed in different (111)-facets, a larger fraction of OOH is formed on Pd. However, the O–O scission rate is low over these sites, preserving a high selectivity. The situation is changed when a Pd monomer is placed on an edge of the nanoparticle. In this case, OOH is to a large extent formed on Pd, due to the strong O_2 adsorption energy on low-coordinated Pd, and facile O–O bond scission, resulting in the formation of H_2O. The selectivity cannot be restored by the inclusion of a Pd monomer in a (111)-facet, over which the selectivity is high, as the adsorption strength of O_2 is weak. The selectivity can, however, be improved by increasing H_2 pressure, effectively blocking ill-located Pd monomers from O_2 adsorption. An optimal catalyst for high H_2O_2 selectivity should only have Pd monomers in (111)-facets, with a large ratio between low-coordinated Au sites and Pd monomers.

5.4 Catalytic reactions over dynamic dilute nanoalloys

The activity towards H_2O_2 over dilute PdAu relies on Pd monomers located in the surface of the nanoparticles. This is a challenge, as the thermodynamically preferred positions of Pd monomers in an inert atmosphere are in the bulk of Au [196, 197]. In a reactive atmosphere, however, the thermodynamic preference is switched to Pd residing in the Au surface, owing to a stronger adsorption energy on Pd [69, 196, 197].

During reaction, there is not a one-to-one correspondence between the thermodynamically preferred compositions and the actual composition of the nanoparti-

cles, as structural changes could be kinetically limited. In the direct formation of H_2O_2 over dilute PdAu, the active catalyst is a meta-stable configuration in inert atmospheres, rather than the thermodynamically preferred state. To investigate the structural evolution of the nanoparticles in inert and reactive environments, a three-dimensional kinetic Monte Carlo approach is constructed in **Paper III**. The possible events in the simulations are expanded to also include atomic displacements, *i.e.*, changes to the catalytic sites. The update of the system is, in this case, with respect to site coverages and site positions. This approach enables the possibility to simulate the chemistry on the nanoparticle surface, and the structural evolution of the nanoparticle bulk and surface simultaneously. It is found that the deactivation of the catalyst (loss of surface Pd) in an inert atmosphere is slow at low temperatures. This is in agreement with experimental findings where Pd deposited on stepped Au surfaces at 380 K are located mainly in the surface layer, whereas at 460 K they are located sub-surface [198, 199]. The activation of the nanoparticles is thermodynamically enabled in CO atmospheres. However, at low temperatures, the time for activation is long, owing to kinetic limitations. The deactivation and activation of the catalysts rely on the formation of vacancies in the system. In the formation of a vacancy, a surface atom is detached from the surface, forming an ad-atom on the surface. It is found that CO does not only stabilize Pd at the surface, but also increases the formation rate and stability of vacancies and ad-atoms in the nanoparticles. The influence of CO on the formation of a vacancy and an ad-atom in the case of an extended (111)-surface is presented in Figure 5.5.

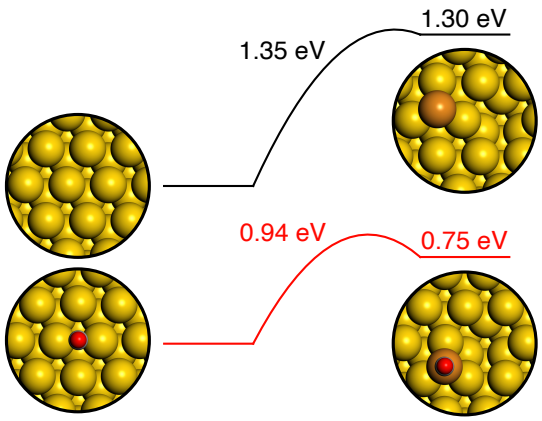

Figure 5.5: The energy barrier and stability for the formation of a vacancy and an ad-atom in (top) inert atmospheres and (bottom) the presence of CO. Atomic color codes: Au (yellow), Au ad-atom (brown), O (red), and C (gray).

The energy barrier to form a vacancy is in inert atmospheres high, and the stability is low. Hence, when a vacancy is formed, it will immediately be healed by

the ad-atom. In the CO-facilitated process, the barrier is reduced by ∼0.4 eV as compared to the inert process. The barrier for the healing of the vacancy is in the presence of CO increased to 0.19 eV, as compared to 0.05 eV in the inert case. The increased barrier for vacancy healing results in an increased coverage of vacancies in the system. The facility of vacancy formation increases with lower coordination of the metal atom, and is the fastest on nanoparticle corners.

The facile ad-atom formation and higher stability of ad-atoms in the presence of CO results in formation of transient clusters on the nanoparticle surface, shown in Figure 5.6. The transient clusters are formed and dispersed on the micro-second time-scale, which makes them difficult to capture with first-principles molecular dynamics simulations or experimental methods. As low-coordinated atoms and clusters could be associated with unique catalytic properties [73, 200, 201], they might be responsible for a large part of the catalytic activity. The kinetic Monte Carlo approach opens up the possibility to also incorporate structural changes of nanocatalysts during reactions.

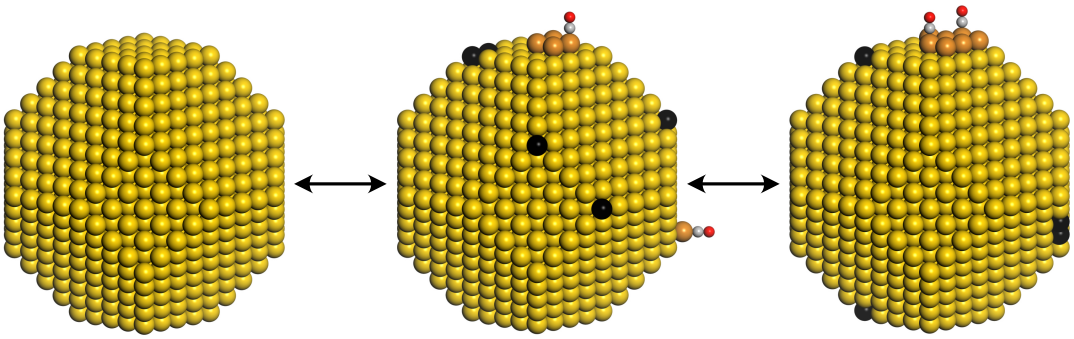

Figure 5.6: Structures obtained from a kinetic Monte Carlo simulation for an Au nanoparticle in a CO-pressure of 1 bar and a temperature of 300 °C. Atomic color codes: Au (yellow), Au ad-atom (brown), O (red), and C (gray). The vacancies are emphasized with black color.

6

Concluding remarks

The objective of this work has been to explore catalytic processes at the atomic scale, with special emphasis on processes occurring in multi-component catalyst systems. Charge transfer phenomena occurring at interfaces between catalyst constituents and the kinetic implications during catalytic reactions, have been investigated with density functional theory calculations and kinetic Monte Carlo simulations. The kinetic implications of metal/metal interplay and the charge separation of hydrogen at the metal/water interface were investigated for the direct formation of H_2O_2 over water-solvated PdAu single-atom alloy nanoparticles. The kinetic Monte Carlo simulations were extended to also explore the structural evolution of nanoparticles in inert and reactive atmospheres. Charge transfer processes at metal/oxide interfaces were explored in the case of H_2 adsorption. The kinetic implications of this process were investigated for the case of CO_2 hydrogenation to methanol over Cu/ZnO catalysts.

In this chapter, the main findings of the work are presented. The limitations of the computational approaches, and possible ways to improve the description of catalytic reactions, are discussed. The chapter is concluded with a brief perspective on future possibilities in continuation of this work.

6.1 Main findings

The reason for the high selectivity towards H_2O_2 in the direct formation from H_2 and O_2 over dilute PdAu nanoparticles in a water solution was found to have several origins. Pd atoms in the surface of the Au nanoparticles act as active centers for H_2 adsorption and dissociation, which is crucial for the reaction to proceed. A

facile charge separation of hydrogen at the metal/water interface, in which a proton is solvated in the water solution, and the electron is transferred to the metal surface, enables a new, faster, reaction path towards H_2O_2. The proton and electron recombine at O_2 species adsorbed on Au sites at the nanoparticle edges and corners, resulting in the formation of H_2O_2. The separation of elementary reaction events for this reaction is a novel mechanism, and is for nanoparticles with Pd atoms located in low-coordinated positions, important to maintain a high selectivity towards H_2O_2.

The charge separation of hydrogen at the metal/water interface is exothermic, or close to thermo-neutral, and associated with small energy barriers also for Pd(111), Ag(111), and Pt(111). At the Cu(111)/water interface, the charge separation has a considerably higher barrier, being 0.85 eV. Water is found to also stabilize the adsorption of O_2 on the metal surfaces, as a result of a metal-to-O_2 charge transfer, increasing the hydrogen bond strengths at the interface. The altered potential energy surface and new reaction pathways enabled at the metal/water interface could have implications also for other hydrogenation reactions occurring in the presence of water.

The kinetic Monte Carlo simulations were extended to explore the structural evolution of Au and PdAu single-atom alloy catalysts in inert and reactive atmospheres. Pd residing in (111)-facets of the Au nanoparticle are meta-stable, and found to not migrate to the bulk at low temperatures. A reactive atmosphere, such as CO, is known to stabilize Pd at the surface of Au. However, the presence of CO also has important consequences for the kinetics of the activation. In the presence of CO, the energy barrier for the formation of a vacancy and an ad-atom is reduced and the formed ad-atom is stabilized. The adsorbate-induced increase of vacancies is important for Pd migration to the surface. The presence of CO also gives rise to the formation of transient cluster on the nanoparticle surface. The transient clusters are formed during reaction conditions, and could have important implications for catalytic reactions occurring at low-coordinated sites.

The metal/oxide interface was investigated for metal nanoparticles supported on ZnO, MgO, and ZrO_2 surfaces in the case of H_2 adsorption. Whereas the adsorption is weak on the pristine oxide surfaces, the inclusion of a metal nanoparticle is found to substantially increase the H_2 adsorption strength. The reason for the stabilization of adsorbed H_2 on oxide ions in the oxide is a result of electron transferring to the metal, effectively charging the metal nanoparticles under reaction conditions. The metal/oxide synergy results in OH-groups close to the metal during reaction. The OH-groups could potentially form hydrogen bonds with intermediates at the metal/oxide interface, or act as a hydrogen buffer during hydrogenation reactions.

The kinetic implications of the metal/oxide synergy are investigated for CO_2 hydrogenation to methanol over Cu nanoparticles supported on ZnO. The H_2-induced charge transfer to the Cu nanoparticles could influence the stability of intermediates on the metal surface. For the C−O bond breaking in HCOOH, forming HCO and OH, the charge transfer results in a 0.1 eV lowering of the energy barrier. Furthermore, the stabilization of hydrogen on ZnO close to the Cu nanoparticles substantially increases the adsorption strength of HCOO at the perimeter of the Cu nanoparticles, owing to hydrogen bonds.

At the metal/oxide interface, oxygen vacancies in the oxide are found to be stabilized, owing to the excess electrons transferring to the metal nanoparticles. This could, *e.g.*, facilitate a Mars-van-Krevelen mechanism during reaction, or other processes which may be sensitive to the presence of oxygen vacancies. Understanding the synergetic interplay at metal/water and metal/oxide interfaces could be an important step in the discovery of efficient catalysts. The synergies give rise to altered potential energy surfaces and enable new reaction pathways, influencing the activity and selectivity in the reaction.

6.2 Limitations

Modeling catalytic reactions is challenging, and the accuracy of the predictions relies on several approximations. A first approximation is the catalyst system itself. As operational catalysts are often complex multi-component materials, simplified catalyst structures are used to model the parts which are believed to be responsible for the catalytic activity. As kinetic models often describe the reaction over a static catalyst, knowledge of structure and chemical state of the catalyst during reaction conditions is valuable. Furthermore, model structures are often small compared to the operational catalyst, which leads to impurities, promoters, or irregular structural defects often being either neglected or overestimated. The simplification of the model system is a trade-off between an accurate description of the catalyst and the computational feasibility.

The kinetics of a catalytic reaction is governed by the potential energy surface, which is obtained from density functional theory calculations. Small errors in the description of relative intermediate stabilities and energy barriers could have large implications for the kinetics. For example, if the free energy barrier of an elementary reaction is changed by 0.2 eV, the elementary reaction rate is altered by a factor ~ 500 at 100 °C. This could be problematic, as the accuracy of the density functional theory calculations rely on the description of the exchange and correla-

tion functional. For the PBE functional, the errors in intermediate stability often exceeds 0.2 eV as compared to experimental results [202]. Fortunately, as the errors of the calculations often scales similarly for intermediates, the differences in errors for an elementary reaction tend to be less uncertain. The relative errors do, however, not cancel in the case of reactant and product energies, which need to be corrected to obtain an accurate prediction of the turn-over frequency.

6.3 Future possibilities

There are many interesting processes to explore in continuation of this work. The description of the dynamic behavior of nanoparticles during reactions can be employed to more complex chemical processes on the catalyst surface. For example, during oxidation reactions where parts of the catalyst could oxidize during reaction, influencing the catalytic activity. The possibility to combine the description of chemical state and structural evolution of a catalyst during reactions is an interesting route. This is, however, challenging, as the configurational space grows substantially for each new intermediate in the reaction. A first step to refine the modeling of chemical reactions on dynamic nanoparticles could be to also include adsorbate-induced strain effects, which may affect chemical processes on the surface, and the structural evolution of the catalyst.

The dynamic description of catalysts could be employed for metal nanoparticles supported on an oxide support. In this case, the structural changes of the particles, potential alloying, and the formation of oxygen vacancies during reactions could be investigated simultaneously. Furthermore, the possible detachment of atoms from the nanoparticle, forming single-atom catalysts on the oxide surface, or Ostwald-ripening processes could be explored. Metal/liquid interfaces could be investigated for other surface orientations and different liquids. In this case, an approach based on machine-learned force fields could potentially be employed to *e.g.*, pre-equilibrate the liquid structure at the interface.

The potential of single-atom alloy catalysts for other reactions, in which the selectivity could benefit from site communication, can be further investigated. However, exploring the kinetics of reactions over nanoparticles with kinetic Monte Carlo simulations is computationally expensive, and is therefore an inefficient way to probe the efficiency of many different catalyst materials. It would, therefore, be interesting to explore in which ways mean-field approximations can be included in the simulations to reduce the computational cost, while maintaining the detailed description of kinetic Monte Carlo simulations.

Acknowledgments

The research presented in this doctoral thesis was performed at the Division of Chemical Physics and the Competence Centre for Catalysis at Chalmers University of Technology, Sweden, between August 2021 and March 2026.

The research was funded by the Swedish Research Council (2020-05191) and (2024-05250). Computational time has been granted by NAISS at NSC (Linköping), and PDC (Stockholm). The Competence Centre for Catalysis (KCK) is hosted by Chalmers University of Technology and is financially supported by the Swedish Energy Agency and the member companies Johnson Matthey, Perstorp, Powercell, Preem, Scania CV, Umicore, and Volvo Group.

I would also like to express my gratitude to:

My supervisor, Professor Henrik Grönbeck. Thank you for giving me the opportunity to explore the exciting world of catalysis. It has been a privilege to learn from your expertise in research in general and catalysis in particular. Understanding catalytic processes is challenging, but many energy barriers have been overcome thanks to your passion for the research that we do and the magnitude of valuable discussions.

My co-supervisor, Professor Anders Hellman. Thank you for your formal and informal guidance.

My examiner, Professor Christoph Langhammer. Thank you for your encouraging words, and valuable experimental insights.

The members of the Division of Chemical Physics. Thank you for the good working environment and the good scientific discussions.

Most importantly, my family. Thank you for always supporting me, and encouraging me in my interests.

Bibliography

[1] M. V. Twigg, Progress and future challenges in controlling automotive exhaust gas emissions, *Appl. Catal. B: Environ.* **70**, 2 (2007).

[2] R. Horn and R. Schlögl, Methane activation by heterogeneous catalysis, *Catal. Lett.* **145**, 23 (2015).

[3] R.-P. Ye, J. Ding, W. Gong, M. D. Argyle, Q. Zhong, Y. Wang, C. K. Russell, Z. Xu, A. G. Russell, Q. Li, *et al.*, CO_2 hydrogenation to high-value products via heterogeneous catalysis, *Nat. Commun.* **10**, 5698 (2019).

[4] H. Schulz, Short history and present trends of Fischer–Tropsch synthesis, *Appl. Catal. A: Gen.* **186**, 3 (1999).

[5] T. L. LeValley, A. R. Richard, and M. Fan, The progress in water gas shift and steam reforming hydrogen production technologies – A review, *Int. J. Hydrog. Energy* **39**, 16983 (2014).

[6] R. J. Lewis and G. J. Hutchings, Recent Advances in the Direct Synthesis of H_2O_2, *ChemCatChem* **11**, 298 (2019).

[7] J. Humphreys, R. Lan, and S. Tao, Development and Recent Progress on Ammonia Synthesis Catalysts for Haber–Bosch Process, *Adv. Energy Sustain. Res.* **2**, 2000043 (2021).

[8] I. Chorkendorff and J. W. Niemantsverdriet, *Concepts of Modern Catalysis and Kinetics* (Wiley-VCH, 2017).

[9] C. Vogt and B. M. Weckhuysen, The concept of active site in heterogeneous catalysis, *Nat. Rev. Chem.* **6**, 89 (2022).

[10] D. S. Potts, D. T. Bregante, J. S. Adams, C. Torres, and D. W. Flaherty, Influence of solvent structure and hydrogen bonding on catalysis at solid–liquid interfaces, *Chem. Soc. Rev.* **50**, 12308 (2021).

[11] C. H. Bartholomew, Mechanisms of catalyst deactivation, *Appl. Catal. A: Gen.* **212**, 17 (2001).

[12] H. Swenson and N. P. Stadie, Langmuir's Theory of Adsorption: A Centennial Review, *Langmuir* **35**, 5409 (2019).

[13] H. Eyring, The Activated Complex in Chemical Reactions, *J. Chem. Phys.* **3**, 107 (1935).

[14] K. W. Kolasinski, *Surface Science: Foundations of Catalysis and Nanoscience* (John Wiley & Sons, 2002).

[15] G. Binnig and H. Rohrer, Scanning tunneling microscopy—from birth to adolescence, *Rev. Mod. Phys.* **59**, 615 (1987).

[16] K. Siegbahn, Electron spectroscopy for atoms, molecules, and condensed matter, *Rev. Mod. Phys.* **54**, 709 (1982).

[17] A. Zangwill, *Physics at surfaces* (Cambridge University Press, 1988).

[18] P. L. Hansen, J. B. Wagner, S. Helveg, J. R. Rostrup-Nielsen, B. S. Clausen, and H. Topsøe, Atom-Resolved Imaging of Dynamic Shape Changes in Supported Copper Nanocrystals, *Science* **295**, 2053 (2002).

[19] F. Tao, M. E. Grass, Y. Zhang, D. R. Butcher, J. R. Renzas, Z. Liu, J. Y. Chung, B. S. Mun, M. Salmeron, and G. A. Somorjai, Reaction-Driven Restructuring of Rh-Pd and Pt-Pd Core-Shell Nanoparticles, *Science* **322**, 932 (2008).

[20] B. Eren, D. Zherebetskyy, L. L. Patera, C. H. Wu, H. Bluhm, C. Africh, L.-W. Wang, G. A. Somorjai, and M. Salmeron, Activation of Cu(111) surface by decomposition into nanoclusters driven by CO adsorption, *Science* **351**, 475 (2016).

[21] G. H. Simon, C. S. Kley, and B. Roldan Cuenya, Potential-Dependent Morphology of Copper Catalysts During CO_2 Electroreduction Revealed by In Situ Atomic Force Microscopy, *Angew. Chem. Int. Ed.* **60**, 2561 (2021).

[22] J. Timoshenko, A. Bergmann, C. Rettenmaier, A. Herzog, R. M. Arán-Ais, H. S. Jeon, F. T. Haase, U. Hejral, P. Grosse, S. Kühl, *et al.*, Steering the structure and selectivity of CO_2 electroreduction catalysts by potential pulses, *Nat. Catal.* **5**, 259 (2022).

[23] C. M. Goodwin, P. Lomker, D. Degerman, B. Davies, M. Shipilin, F. Garcia-Martinez, S. Koroidov, J. K. Mathiesen, R. Rameshan, G. L. S. Rodrigues, C. Schlueter, P. Amann, and A. Nilsson, Operando probing of the surface chemistry during the Haber-Bosch process, *Nature* **625**, 282 (2024).

[24] P. W. Anderson, Localized Magnetic States in Metals, *Phys. Rev.* **124**, 41 (1961).

[25] D. M. Newns, Self-Consistent Model of Hydrogen Chemisorption, *Phys. Rev.* **178**, 1123 (1969).

[26] R. Hoffmann, *Solids and surfaces : a chemist's view of bonding in extended structures* (VCH, 1988).

[27] P. Hohenberg and W. Kohn, Inhomogeneous Electron Gas, *Phys. Rev.* **136**, B864 (1964).

[28] W. Kohn and L. J. Sham, Self-Consistent Equations Including Exchange and Correlation Effects, *Phys. Rev.* **140**, A1133 (1965).

[29] J. P. Perdew and Y. Wang, Accurate and simple analytic representation of the electron-gas correlation energy, *Phys. Rev. B* **45**, 13244 (1992).

[30] A. D. Becke, A new mixing of Hartree–Fock and local density-functional theories, *J. Chem. Phys.* **98**, 1372 (1993).

[31] B. Hammer and J. Nørskov, why gold is the noblest of all the metals, *Nature* **376**, 238 (1995).

[32] B. Hammer and J. Nørskov, Electronic factors determining the reactivity of metal surfaces, *Surf. Sci.* **343**, 211 (1995).

[33] B. Hammer, Y. Morikawa, and J. K. Nørskov, CO Chemisorption at Metal Surfaces and Overlayers, *Phys. Rev. Lett.* **76**, 2141 (1996).

[34] M. Mavrikakis, B. Hammer, and J. K. Nørskov, Effect of Strain on the Reactivity of Metal Surfaces, *Phys. Rev. Lett.* **81**, 2819 (1998).

[35] T. Bligaard, J. Nørskov, S. Dahl, J. Matthiesen, C. Christensen, and J. Sehested, The Brønsted–Evans–Polanyi relation and the volcano curve in heterogeneous catalysis, *J. Catal.* **224**, 206 (2004).

[36] P. Stoltze and J. K. Nørskov, Bridging the "Pressure Gap" between Ultrahigh-Vacuum Surface Physics and High-Pressure Catalysis, *Phys. Rev. Lett.* **55**, 2502 (1985).

[37] O. R. Inderwildi, S. J. Jenkins, and D. A. King, An Unexpected Pathway for the Catalytic Oxidation of Methylidyne on Rh{111} as a Route to Syngas, *J. Am. Chem. Soc.* **129**, 1751 (2007).

[38] L. C. Grabow, A. A. Gokhale, S. T. Evans, J. A. Dumesic, and M. Mavrikakis, Mechanism of the Water Gas Shift Reaction on Pt: First Principles, Experiments, and Microkinetic Modeling, *J. Phys. Chem. C* **112**, 4608 (2008).

[39] A. A. Gokhale, J. A. Dumesic, and M. Mavrikakis, On the Mechanism of Low-Temperature Water Gas Shift Reaction on Copper, *J. Am. Chem. Soc.* **130**, 1402 (2008).

[40] D. A. Hansgen, D. G. Vlachos, and J. G. Chen, Using first principles to predict bimetallic catalysts for the ammonia decomposition reaction, *Nat. Chem.* **2**, 484 (2010).

[41] I. A. W. Filot, R. A. van Santen, and E. J. M. Hensen, The Optimally Performing Fischer–Tropsch Catalyst, *Angew. Chem. Int. Ed.* **53**, 12746 (2014).

[42] M. Van den Bossche and H. Grönbeck, Methane Oxidation over PdO(101) Revealed by First-Principles Kinetic Modeling, *J. Am. Chem. Soc.* **137**, 12035 (2015).

[43] A. R. Singh, J. H. Montoya, B. A. Rohr, C. Tsai, A. Vojvodic, and J. K. Nørskov, Computational Design of Active Site Structures with Improved Transition-State Scaling for Ammonia Synthesis, *ACS Catal.* **8**, 4017 (2018).

[44] L. Chen, J. W. Medlin, and H. Grönbeck, On the Reaction Mechanism of Direct H_2O_2 Formation over Pd Catalysts, *ACS Catal.* **11**, 2735 (2021).

[45] B. W. J. Chen, L. Xu, and M. Mavrikakis, Computational Methods in Heterogeneous Catalysis, *Chem. Rev.* **121**, 1007 (2021).

[46] M. Stamatakis and D. G. Vlachos, Unraveling the Complexity of Catalytic Reactions via Kinetic Monte Carlo Simulation: Current Status and Frontiers, *ACS Catal.* **2**, 2648 (2012).

[47] D. Mei, P. A. Sheth, M. Neurock, and C. M. Smith, First-principles-based kinetic Monte Carlo simulation of the selective hydrogenation of acetylene over Pd(111), *J. Catal.* **242**, 1 (2006).

[48] K. Reuter and M. Scheffler, First-principles kinetic Monte Carlo simulations for heterogeneous catalysis: Application to the CO oxidation at RuO_2(110), *Phys. Rev. B* **73**, 045433 (2006).

[49] J. Rogal, K. Reuter, and M. Scheffler, CO oxidation on Pd(100) at technologically relevant pressure conditions: First-principles kinetic Monte Carlo study, *Phys. Rev. B* **77**, 155410 (2008).

[50] D. Mei, M. Neurock, and C. M. Smith, Hydrogenation of acetylene–ethylene mixtures over Pd and Pd–Ag alloys: First-principles-based kinetic Monte Carlo simulations, *J. Catal.* **268**, 181 (2009).

[51] M. Stamatakis, Y. Chen, and D. G. Vlachos, First-Principles-Based Kinetic Monte Carlo Simulation of the Structure Sensitivity of the Water–Gas Shift Reaction on Platinum Surfaces, *J. Phys. Chem. C* **115**, 24750 (2011).

[52] S. Piccinin and M. Stamatakis, CO Oxidation on Pd(111): A First-Principles-Based Kinetic Monte Carlo Study, *ACS Catal.* **4**, 2143 (2014).

[53] H. Prats, P. Gamallo, F. Illas, and R. Sayós, Comparing the catalytic activity of the water gas shift reaction on Cu(321) and Cu(111) surfaces: Step sites do not always enhance the overall reactivity, *J. Catal.* **342**, 75 (2016).

[54] H.-J. Chun, V. Apaja, A. Clayborne, K. Honkala, and J. Greeley, Atomistic Insights into Nitrogen-Cycle Electrochemistry: A Combined DFT and Kinetic Monte Carlo Analysis of NO Electrochemical Reduction on Pt(100), *ACS Catal.* **7**, 3869 (2017).

[55] F. Hess and H. Over, Rate-Determining Step or Rate-Determining Configuration? The Deacon Reaction over RuO_2(110) Studied by DFT-Based KMC Simulations, *ACS Catal.* **7**, 128 (2017).

[56] M. Jørgensen and H. Grönbeck, The Site-Assembly Determines Catalytic Activity of Nanoparticles, *Angew. Chem. Int. Ed.* **57**, 5086 (2018).

[57] M. Jørgensen and H. Grönbeck, Selective Acetylene Hydrogenation over Single-Atom Alloy Nanoparticles by Kinetic Monte Carlo, *J. Am. Chem. Soc.* **141**, 8541 (2019).

[58] A. Chutia, A. Thetford, M. Stamatakis, and C. R. A. Catlow, A DFT and KMC based study on the mechanism of the water gas shift reaction on the Pd(100) surface, *Phys. Chem. Chem. Phys.* **22**, 3620 (2020).

[59] H. Prats and M. Stamatakis, First-Principles Kinetic Monte Carlo Simulations for Single-Cluster Catalysis: Study of CO_2 and CH_4 Conversion on Pt/HfC, *ACS Catal.* **15**, 2904 (2025).

[60] S. Ringe, N. G. Hörmann, H. Oberhofer, and K. Reuter, Implicit Solvation Methods for Catalysis at Electrified Interfaces, *Chem. Rev.* **122**, 10777 (2022).

[61] C. Sievers, Y. Noda, L. Qi, E. M. Albuquerque, R. M. Rioux, and S. L. Scott, Phenomena Affecting Catalytic Reactions at Solid–Liquid Interfaces, *ACS Catal.* **6**, 8286 (2016).

[62] D. S. Potts, D. T. Bregante, J. S. Adams, C. Torres, and D. W. Flaherty, Influence of solvent structure and hydrogen bonding on catalysis at solid-liquid interfaces, *Chem. Soc. Rev.* **50**, 12308 (2021).

[63] A. Ruiz Puigdollers, P. Schlexer, S. Tosoni, and G. Pacchioni, Increasing Oxide Reducibility: The Role of Metal/Oxide Interfaces in the Formation of Oxygen Vacancies, *ACS Catal.* **7**, 6493 (2017).

[64] T. W. van Deelen, C. H. Mejia, and K. P. de Jong, Control of metal-support interactions in heterogeneous catalysts to enhance activity and selectivity, *Nat. Catal.* **2**, 955 (2019).

[65] D. Leybo, U. J. Etim, M. Monai, S. R. Bare, Z. Zhong, and C. Vogt, Metal-support interactions in metal oxide-supported atomic, cluster, and nanoparticle catalysis, *Chem. Soc. Rev.* **53**, (2024).

[66] J.-D. Grunwaldt, A. Molenbroek, N.-Y. Topsøe, H. Topsøe, and B. Clausen, In Situ Investigations of Structural Changes in Cu/ZnO Catalysts, *J. Catal.* **194**, 452 (2000).

[67] F. F. Tao, L. Nguyen, S. Zhang, Y. Li, Y. Tang, L. Zhang, A. I. Frenkel, Y. Xia, and M. Salmeron, Formation of Second-Generation Nanoclusters on Metal Nanoparticles Driven by Reactant Gases, *Nano Lett.* **16**, 5001 (2016).

[68] A. Ricchebuono, E. Vottero, D. Bonavia, P. Lazzarini, R. Pellegrini, V. Crocellà, N. G. Porcaro, S. Checchia, D. Ferri, A. Piovano, and E. Groppo, CO-Induced Dynamic Behavior of Al_2O_3-Supported Pd Nanoparticles at Room Temperature, *ACS Catal.* **14**, 13736 (2024).

[69] M. Luneau, E. Guan, W. Chen, A. C. Foucher, N. Marcella, T. Shirman, D. M. A. Verbart, J. Aizenberg, M. Aizenberg, E. A. Stach, R. J. Madix, A. Frenkel, I, and C. M. Friend, Enhancing catalytic performance of dilute metal alloy nanomaterials, *Commun. Chem.* **3**, (2020).

[70] Y.-G. Wang, D. Mei, V.-A. Glezakou, J. Li, and R. Rousseau, Dynamic formation of single-atom catalytic active sites on ceria-supported gold nanoparticles, *Nat. Commun.* **6**, (2015).

[71] K. McCrea, J. S. Parker, P. Chen, and G. Somorjai, Surface structure sensitivity of high-pressure CO dissociation on Pt(557), Pt(100) and Pt(111) using sum frequency generation surface vibrational spectroscopy, *Surf. Sci.* **494**, 238 (2001).

[72] F. Tao, S. Dag, L.-W. Wang, Z. Liu, D. R. Butcher, H. Bluhm, M. Salmeron, and G. A. Somorjai, Break-Up of Stepped Platinum Catalyst Surfaces by High CO Coverage, *Science* **327**, 850 (2010).

[73] L. Xu, K. G. Papanikolaou, B. A. J. Lechner, L. Je, G. A. Somorjai, M. Salmeron, and M. Mavrikakis, Formation of active sites on transition metals through reaction-driven migration of surface atoms, *Science* **380**, 70 (2023).

[74] J. M. Campos-Martin, G. Blanco-Brieva, and J. L. G. Fierro, Hydrogen Peroxide Synthesis: An Outlook beyond the Anthraquinone Process, *Angew. Chem. Int. Ed.* **45**, 6962 (2006).

[75] R. Hage and A. Lienke, Applications of Transition-Metal Catalysts to Textile and Wood-Pulp Bleaching, *Angew. Chem. Int. Ed.* **45**, 206 (2006).

[76] M. Pera-Titus, V. García-Molina, M. A. Baños, J. Giménez, and S. Esplugas, Degradation of chlorophenols by means of advanced oxidation processes: a general review, *Appl. Catal. B: Environ.* **47**, 219 (2004).

[77] R. J. Lewis, K. Ueura, X. Liu, Y. Fukuta, T. E. Davies, D. J. Morgan, L. Chen, J. Qi, J. Singleton, J. K. Edwards, S. J. Freakley, C. J. Kiely, Y. Yamamoto, and

G. J. Hutchings, Highly efficient catalytic production of oximes from ketones using in situ generated H_2O_2, *Science* **376**, 615 (2022).

[78] R. J. Lewis and G. J. Hutchings, Recent Advances in the Direct Synthesis of H_2O_2, *ChemCatChem* **11**, 298 (2019).

[79] N. M. Wilson and D. W. Flaherty, Mechanism for the Direct Synthesis of H_2O_2 on Pd Clusters: Heterolytic Reaction Pathways at the Liquid–Solid Interface, *J. Am. Chem. Soc.* **138**, 574 (2016).

[80] D. P. Dissanayake and J. H. Lunsford, The direct formation of H_2O_2 from H_2 and O_2 over colloidal palladium, *J. Catal.* **214**, 113 (2003).

[81] S. Chinta and J. H. Lunsford, A mechanistic study of H_2O_2 and H_2O formation from H_2 and O_2 catalyzed by palladium in an aqueous medium, *J. Catal.* **225**, 249 (2004).

[82] G. M. Lari, B. Puértolas, M. Shahrokhi, N. López, and J. Pérez-Ramírez, Hybrid Palladium Nanoparticles for Direct Hydrogen Peroxide Synthesis: The Key Role of the Ligand, *Angew. Chem. Int. Ed.* **56**, 1775 (2017).

[83] D. W. Flaherty, Direct Synthesis of H_2O_2 from H_2 and O_2 on Pd Catalysts: Current Understanding, Outstanding Questions, and Research Needs, *ACS Catal.* **8**, 1520 (2018).

[84] L. Chen, P. Moura, J. W. Medlin, and H. Grönbeck, Multiple Roles of Alkanethiolate-Ligands in Direct Formation of H_2O_2 over Pd Nanoparticles, *Angew. Chem. Int. Ed.* **61**, e202213113 (2022).

[85] J. K. Edwards, B. Solsona, E. Ntainjua N, A. F. Carley, A. A. Herzing, C. J. Kiely, and G. J. Hutchings, Switching Off Hydrogen Peroxide Hydrogenation in the Direct Synthesis Process, *Science* **323**, 1037 (2009).

[86] T. Whittaker, K. B. S. Kumar, C. Peterson, M. N. Pollock, L. C. Grabow, and B. D. Chandler, H_2 Oxidation over Supported Au Nanoparticle Catalysts: Evidence for Heterolytic H_2 Activation at the Metal–Support Interface, *J. Am. Chem. Soc.* **140**, 16469 (2018).

[87] J. S. Adams, H. Chen, T. Ricciardulli, S. Vijayaraghavan, A. Sampath, and D. W. Flaherty, Distinct Site Motifs Activate O_2 and H_2 on Supported Au Nanoparticles in Liquid Water, *ACS Catal.* **14**, 3248 (2024).

[88] J. K. Edwards, E. Ntainjua N, A. F. Carley, A. A. Herzing, C. J. Kiely, and G. J. Hutchings, Direct Synthesis of H_2O_2 from H_2 and O_2 over Gold, Palladium, and Gold–Palladium Catalysts Supported on Acid-Pretreated TiO_2, *Angew. Chem. Int. Ed.* **48**, 8512 (2009).

[89] J. K. Edwards, B. E. Solsona, P. Landon, A. F. Carley, A. Herzing, C. J. Kiely, and G. J. Hutchings, Direct synthesis of hydrogen peroxide from H_2 and O_2 using TiO_2-supported Au–Pd catalysts, *J. Catal.* **236**, 69 (2005).

[90] T. Ricciardulli, S. Gorthy, J. S. Adams, C. Thompson, A. M. Karim, M. Neurock, and D. W. Flaherty, Effect of Pd Coordination and Isolation on the Catalytic Reduction of O_2 to H_2O_2 over PdAu Bimetallic Nanoparticles, *J. Am. Chem. Soc.* **143**, 5445 (2021).

[91] G. A. Olah, G. K. S. Prakash, and A. Goeppert, Anthropogenic Chemical Carbon Cycle for a Sustainable Future, *J. Am. Chem. Soc.* **133**, 12881 (2011).

[92] A. Goeppert, M. Czaun, J.-P. Jones, G. K. S. Prakash, and G. A. Olah, Recycling of carbon dioxide to methanol and derived products - closing the loop, *Chem. Soc. Rev.* **43**, 7995 (2014).

[93] A. Álvarez, A. Bansode, A. Urakawa, A. V. Bavykina, T. A. Wezendonk, M. Makkee, J. Gascon, and F. Kapteijn, Challenges in the Greener Production of Formates/Formic Acid, Methanol, and DME by Heterogeneously Catalyzed CO_2 Hydrogenation Processes, *Chem. Rev.* **117**, 9804 (2017).

[94] X. Jiang, X. Nie, X. Guo, C. Song, and J. G. Chen, Recent Advances in Carbon Dioxide Hydrogenation to Methanol via Heterogeneous Catalysis, *Chem. Rev.* **120**, 7984 (2020).

[95] J. Ye, N. Dimitratos, L. M. Rossi, N. Thonemann, A. M. Beale, and R. Wojcieszak, Hydrogenation of CO_2 for sustainable fuel and chemical production, *Science* **387**, eadn9388 (2025).

[96] O. Martin, A. J. Martín, C. Mondelli, S. Mitchell, T. F. Segawa, R. Hauert, C. Drouilly, D. Curulla-Ferré, and J. Pérez-Ramírez, Indium Oxide as a Superior Catalyst for Methanol Synthesis by CO_2 Hydrogenation, *Angew. Chem. Int. Ed.* **55**, 6261 (2016).

[97] M. S. Frei, C. Mondelli, R. Garcia-Muelas, K. S. Kley, B. Puertolas, N. Lopez, O. Safonova, V, J. A. Stewart, D. C. Ferre, and J. Perez-Ramirez, Atomic-scale engineering of indium oxide promotion by palladium for methanol production via CO_2 hydrogenation, *Nat. Commun.* **10**, (2019).

[98] J. L. Snider, V. Streibel, M. A. Hubert, T. S. Choksi, E. Valle, D. C. Upham, J. Schumann, M. S. Duyar, A. Gallo, F. Abild-Pedersen, and T. F. Jaramillo, Revealing the Synergy between Oxide and Alloy Phases on the Performance of Bimetallic In–Pd Catalysts for CO_2 Hydrogenation to Methanol, *ACS Catal.* **9**, 3399 (2019).

[99] M. Kauppinen, A. Posada-Borbón, and H. Grönbeck, Methanol Synthesis Over PdIn, In_2O_3, and CuZn From First-Principles Microkinetics: Similarities and Differences, *J. Phys. Chem. C* **126**, 15235 (2022).

[100] J. Graciani, K. Mudiyanselage, F. Xu, A. E. Baber, J. Evans, S. D. Senanayake, D. J. Stacchiola, P. Liu, J. Hrbek, J. F. Sanz, and J. A. Rodriguez, Highly active copper-ceria and copper-ceria-titania catalysts for methanol synthesis from CO_2, *Science* **345**, 546 (2014).

[101] M. Nikolajsen, J.-C. Grivel, A. Gaur, L. Hansen, L. Baumgarten, N. Schjødt, U. Mentzel, J.-D. Grunwaldt, J. Sehested, J. Christensen, and M. Høj, Surface ZnO_x on zirconia is highly active for high temperature methanol synthesis, *J. Catal.* **431**, 115389 (2024).

[102] M. Behrens, F. Studt, I. Kasatkin, S. Kühl, M. Hävecker, F. Abild-Pedersen, S. Zander, F. Girgsdies, P. Kurr, B.-L. Kniep, M. Tovar, R. W. Fischer, J. K. Nørskov,

and R. Schlögl, The Active Site of Methanol Synthesis over $Cu/ZnO/Al_2O_3$ Industrial Catalysts, *Science* **336**, 893 (2012).

[103] F. Studt, M. Behrens, E. L. Kunkes, N. Thomas, S. Zander, A. Tarasov, J. Schumann, E. Frei, J. B. Varley, F. Abild-Pedersen, J. K. Nørskov, and R. Schlögl, The Mechanism of CO and CO_2 Hydrogenation to Methanol over Cu-Based Catalysts, *ChemCatChem* **7**, 1105 (2015).

[104] N. D. Nielsen, A. D. Jensen, and J. M. Christensen, The roles of CO and CO_2 in high pressure methanol synthesis over Cu-based catalysts, *J. Catal.* **393**, 324 (2021).

[105] G. Pacchioni, From CO_2 to Methanol on $Cu/ZnO/Al_2O_3$ Industrial Catalyst. What Do We Know about the Active Phase and the Reaction Mechanism?, *ACS Catal.* **14**, 2730 (2024).

[106] I. Kasatkin, P. Kurr, B. Kniep, A. Trunschke, and R. Schloegl, Role of lattice strain and defects in copper particles on the activity of $Cu/ZnO/Al_2O_3$ catalysts for methanol synthesis, *Angew. Chem. Int. Ed.* **46**, 7324 (2007).

[107] T. Lunkenbein, J. Schumann, M. Behrens, R. Schlögl, and M. G. Willinger, Formation of a ZnO Overlayer in Industrial $Cu/ZnO/Al_2O_3$ Catalysts Induced by Strong Metal–Support Interactions, *Angew. Chem. Int. Ed.* **54**, 4544 (2015).

[108] S. Kuld, M. Thorhauge, H. Falsig, C. F. Elkjær, S. Helveg, I. Chorkendorff, and J. Sehested, Quantifying the promotion of Cu catalysts by ZnO for methanol synthesis, *Science* **352**, 969 (2016).

[109] R. Svensson, *Direct H_2O_2 synthesis over dilute PdAu alloys* (Chalmers University of Technology, 2024).

[110] E. Engel and R. M. Dreizler, *Density Functional Theory: An Advanced Course* (Springer, 2011).

[111] J. Kohanoff, *Electronic Structure Calculations for Solids and Molecules: Theory and Computational Methods* (Cambridge University Press, 2006).

[112] R. O. Jones and O. Gunnarsson, The density functional formalism, its applications and prospects, *Rev. Mod. Phys.* **61**, 689 (1989).

[113] R. M. Martin, *Electronic Structure: Basic Theory and Practical Methods* (Cambridge University Press, 2010).

[114] D. M. Ceperley and B. J. Alder, Ground State of the Electron Gas by a Stochastic Method, *Phys. Rev. Lett.* **45**, 566 (1980).

[115] M. Ernzerhof and G. E. Scuseria, Assessment of the Perdew–Burke–Ernzerhof exchange-correlation functional, *J. Chem. Phys.* **110**, 5029 (1999).

[116] A. D. Becke, Density-functional exchange-energy approximation with correct asymptotic behavior, *Phys. Rev. A* **38**, 3098 (1988).

[117] J. P. Perdew, K. Burke, and M. Ernzerhof, Generalized Gradient Approximation Made Simple, *Phys. Rev. Lett.* **77**, 3865 (1996).

[118] B. Hammer, L. B. Hansen, and J. K. Nørskov, Improved adsorption energetics within density-functional theory using revised Perdew-Burke-Ernzerhof functionals, *Phys. Rev. B* **59**, 7413 (1999).

[119] R. Armiento and A. E. Mattsson, Functional designed to include surface effects in self-consistent density functional theory, *Phys. Rev. B* **72**, 085108 (2005).

[120] J. P. Perdew, A. Ruzsinszky, G. I. Csonka, O. A. Vydrov, G. E. Scuseria, L. A. Constantin, X. Zhou, and K. Burke, Restoring the Density-Gradient Expansion for Exchange in Solids and Surfaces, *Phys. Rev. Lett.* **100**, 136406 (2008).

[121] M. Dion, H. Rydberg, E. Schröder, D. C. Langreth, and B. I. Lundqvist, Van der Waals Density Functional for General Geometries, *Phys. Rev. Lett.* **92**, 246401 (2004).

[122] T. Thonhauser, V. R. Cooper, S. Li, A. Puzder, P. Hyldgaard, and D. C. Langreth, Van der Waals density functional: Self-consistent potential and the nature of the van der Waals bond, *Phys. Rev. B* **76**, 125112 (2007).

[123] K. Berland and P. Hyldgaard, Exchange functional that tests the robustness of the plasmon description of the van der Waals density functional, *Phys. Rev. B* **89**, 035412 (2014).

[124] S. Grimme, J. Antony, S. Ehrlich, and H. Krieg, A consistent and accurate ab initio parametrization of density functional dispersion correction (DFT-D) for the 94 elements H-Pu, *J. Chem. Phys.* **132**, 154104 (2010).

[125] B. Himmetoglu, A. Floris, S. de Gironcoli, and M. Cococcioni, Hubbard-corrected DFT energy functionals: The LDA+U description of correlated systems, *Int. J. Quantum Chem.* **114**, 14 (2014).

[126] A. V. Krukau, O. A. Vydrov, A. F. Izmaylov, and G. E. Scuseria, Influence of the exchange screening parameter on the performance of screened hybrid functionals, *J. Chem. Phys.* **125**, 224106 (2006).

[127] V. I. Anisimov, J. Zaanen, and O. K. Andersen, Band theory and Mott insulators: Hubbard U instead of Stoner I, *Phys. Rev. B* **44**, 943 (1991).

[128] G. Makov and M. C. Payne, Periodic boundary conditions in ab initio calculations, *Phys. Rev. B* **51**, 4014 (1995).

[129] P. E. Blöchl, Projector augmented-wave method, *Phys. Rev. B* **50**, 17953 (1994).

[130] G. Kresse and D. Joubert, From ultrasoft pseudopotentials to the projector augmented-wave method, *Phys. Rev. B* **59**, 1758 (1999).

[131] R. P. Feynman, Forces in Molecules, *Phys. Rev.* **56**, 340 (1939).

[132] J. K. Nørskov, F. Studt, F. Abild-Pedersen, and T. Bligaard, *Fundamental concepts in heterogeneous catalysis* (John Wiley & Sons, 2014).

[133] G. Henkelman and H. Jónsson, Improved tangent estimate in the nudged elastic band method for finding minimum energy paths and saddle points, *J. Chem. Phys.* **113**, 9978 (2000).

[134] G. Henkelman and H. Jónsson, A dimer method for finding saddle points on high dimensional potential surfaces using only first derivatives, *J. Chem. Phys.* **111**, 7010 (1999).

[135] G. Henkelman, B. P. Uberuaga, and H. Jónsson, A climbing image nudged elastic band method for finding saddle points and minimum energy paths, *J. Chem. Phys.* **113**, 9901 (2000).

[136] M. P. Allen and D. J. Tildesley, *Computer Simulation of Liquids* (Oxford University Press, 2009).

[137] J.-P. Ryckaert, G. Ciccotti, and H. J. Berendsen, Numerical integration of the cartesian equations of motion of a system with constraints: molecular dynamics of n-alkanes, *J. Comput. Phys.* **23**, 327 (1977).

[138] M. Sprik and G. Ciccotti, Free energy from constrained molecular dynamics, *J. Chem. Phys.* **109**, 7737 (1998).

[139] E. Carter, G. Ciccotti, J. T. Hynes, and R. Kapral, Constrained reaction coordinate dynamics for the simulation of rare events, *Chem. Phys. Lett.* **156**, 472 (1989).

[140] M. Jørgensen and H. Grönbeck, Adsorbate Entropies with Complete Potential Energy Sampling in Microkinetic Modeling, *J. Phys. Chem. C* **121**, 7199 (2017).

[141] A. P. J. Jansen, *An Introduction to Kinetic Monte Carlo Simulations of Surface Reactions* (Springer, 2012).

[142] D. V. Schroeder, *An Introduction to Thermal Physics* (Addison Wesley Longman, 2000).

[143] A. Hellman, B. Razaznejad, and B. I. Lundqvist, Trends in sticking and adsorption of diatomic molecules on the Al(111) surface, *Phys. Rev. B* **71**, 205424 (2005).

[144] D. T. Gillespie, A general method for numerically simulating the stochastic time evolution of coupled chemical reactions, *J. Comput. Phys.* **22**, 403 (1976).

[145] K. A. Fichthorn and W. H. Weinberg, Theoretical foundations of dynamical Monte Carlo simulations, *J. Chem. Phys.* **95**, 1090 (1991).

[146] M. Jørgensen and H. Grönbeck, Perspectives on Computational Catalysis for Metal Nanoparticles, *ACS Catal.* **9**, 8872 (2019).

[147] M. Pineda and M. Stamatakis, Kinetic Monte Carlo simulations for heterogeneous catalysis: Fundamentals, current status, and challenges, *J. Chem. Phys.* **156**, 120902 (2022).

[148] M. Jørgensen and H. Grönbeck, MonteCoffee: A programmable kinetic Monte Carlo framework, *J. Chem. Phys.* **149**, 114101 (2018).

[149] R. B. Getman and W. F. Schneider, DFT-Based Coverage-Dependent Model of Pt-Catalyzed NO Oxidation, *ChemCatChem* **2**, 1450 (2010).

[150] L. C. Grabow, A. A. Gokhale, S. T. Evans, J. A. Dumesic, and M. Mavrikakis, Mechanism of the Water Gas Shift Reaction on Pt: First Principles, Experiments, and Microkinetic Modeling, *J. Phys. Chem. C* **112**, 4608 (2008).

[151] S. D. Miller and J. R. Kitchin, Uncertainty and figure selection for DFT based cluster expansions for oxygen adsorption on Au and Pt (111) surfaces, *Mol. Simul.* **35**, 920 (2009).

[152] D. J. Schmidt, W. Chen, C. Wolverton, and W. F. Schneider, Performance of Cluster Expansions of Coverage-Dependent Adsorption of Atomic Oxygen on Pt(111), *J. Chem. Theory Comput.* **8**, 264 (2012).

[153] W. Vanmoerkerke, R. Svensson, and H. Grönbeck, Efficient parameterization of adsorbate–adsorbate interactions on metal surfaces, *Surf. Sci.* **754**, 122678 (2025).

[154] N. Bosio, M. Di, M. Skoglundh, P.-A. Carlsson, and H. Grönbeck, Interface Reactions Dominate Low-Temperature CO Oxidation Activity over Pt/CeO_2, *J. Phys. Chem. C* **126**, 16164 (2022).

[155] S. Han, E. J. Evans, Jr., G. M. Mullen, and C. B. Mullins, H_2O-Improved O_2 activation on the Pd-Au bimetallic surface, *Chem. Commun.* **53**, 3990 (2017).

[156] M. Valter, B. Wickman, and A. Hellman, Solvent Effects for Methanol Electrooxidation on Gold, *J. Phys. Chem. C* **125**, 1355 (2021).

[157] B. N. Zope, D. D. Hibbitts, M. Neurock, and R. J. Davis, Reactivity of the Gold/Water Interface During Selective Oxidation Catalysis, *Science* **330**, 74 (2010).

[158] J. S. Adams, A. Chemburkar, P. Priyadarshini, T. Ricciardulli, Y. Lu, V. Maliekkal, A. Sampath, S. Winikoff, A. M. Karim, M. Neurock, and D. W. Flaherty, Solvent molecules form surface redox mediators in situ and cocatalyze O_2 reduction on Pd, *Science* **371**, 626 (2021).

[159] D. Lackey, J. Schott, J. Sass, S. Woo, and F. Wagner, Surface-science simulation study of the electrochemical charge-transfer reaction $(H)_{ad} + (H_2O)_{ad} \rightarrow (H_3O^+)_{ad} + e^-_{metal}$ on Pt(111) and Cu(110), *Chem. Phys. Lett.* **184**, 277 (1991).

[160] N. Kizhakevariam and E. Stuve, Coadsorption of water and hydrogen on Pt(100): formation of adsorbed hydronium ions, *Surf. Sci.* **275**, 223 (1992).

[161] M. Pan, Z. D. Pozun, W.-Y. Yu, G. Henkelman, and C. B. Mullins, Structure Revealing H/D Exchange with Co-Adsorbed Hydrogen and Water on Gold, *J. Phys. Chem. Lett.* **3**, 1894 (2012).

[162] J. Heras and L. Viscido, Work function changes upon water contamination of metal surfaces, *Appl. Surf. Sci.* **4**, 238 (1980).

[163] H. L. Skriver and N. M. Rosengaard, Surface energy and work function of elemental metals, *Phys. Rev. B* **46**, 7157 (1992).

[164] L. Chen, J. W. Medlin, and H. Grönbeck, On the Reaction Mechanism of Direct H_2O_2 Formation over Pd Catalysts, *ACS Catal.* **11**, 2735 (2021).

[165] Y. Zhang, R. J. Lewis, Z. Li, X. He, H. Ji, and G. J. Hutchings, Direct Synthesis of H_2O_2 by Spatially Separate Hydrogen and Oxygen Activation Sites on Tailored Pt–Au Catalysts, *Angew. Chem. Int. Ed.* **65**, e21118 (2026).

[166] C.-J. Pan, M.-C. Tsai, W.-N. Su, J. Rick, N. G. Akalework, A. K. Agegnehu, S.-Y. Cheng, and B.-J. Hwang, Tuning/exploiting Strong Metal-Support Interaction (SMSI) in Heterogeneous Catalysis, *J. Taiwan Inst. Chem. Eng.* **74**, 154 (2017).

[167] I. Ro, J. Resasco, and P. Christopher, Approaches for Understanding and Controlling Interfacial Effects in Oxide-Supported Metal Catalysts, *ACS Catal.* **8**, 7368 (2018).

[168] J. Saavedra, H. A. Doan, C. J. Pursell, L. C. Grabow, and B. D. Chandler, The critical role of water at the gold-titania interface in catalytic CO oxidation, *Science* **345**, 1599 (2014).

[169] R. M. Palomino, P. J. Ramírez, Z. Liu, R. Hamlyn, I. Waluyo, M. Mahapatra, I. Orozco, A. Hunt, J. P. Simonovis, S. D. Senanayake, and J. A. Rodriguez, Hy-

drogenation of CO_2 on ZnO/Cu(100) and ZnO/Cu(111) Catalysts: Role of Copper Structure and Metal–Oxide Interface in Methanol Synthesis, *J. Phys. Chem. B* **122**, 794 (2018).

[170] T. N. Pingel, M. Jørgensen, A. B. Yankovich, H. Grönbeck, and E. Olsson, Influence of atomic site-specific strain on catalytic activity of supported nanoparticles, *Nat. Commun.* **9**, (2018).

[171] P. Mars and D. van Krevelen, Oxidations carried out by means of vanadium oxide catalysts, *Chem. Eng. Sci.* **3**, 41 (1954).

[172] G. Pacchioni, L. Giordano, and M. Baistrocchi, Charging of Metal Atoms on Ultrathin MgO/Mo(100) Films, *Phys. Rev. Lett.* **94**, 226104 (2005).

[173] H. Grönbeck, Mechanism for NO_2 Charging on Metal Supported MgO, *J. Phys. Chem. B* **110**, 11977 (2006).

[174] K. Honkala, A. Hellman, and H. Grönbeck, Water Dissociation on MgO/Ag(100): Support Induced Stabilization or Electron Pairing?, *J. Phys. Chem. C* **114**, 7070 (2010).

[175] Y.-N. Sun, L. Giordano, J. Goniakowski, M. Lewandowski, Z.-H. Qin, C. Noguera, S. Shaikhutdinov, G. Pacchioni, and H.-J. Freund, The Interplay between Structure and CO Oxidation Catalysis on Metal-Supported Ultrathin Oxide Films, *Angew. Chem. Int. Ed.* **49**, 4418 (2010).

[176] H.-Y. T. Chen, L. Giordano, and G. Pacchioni, From Heterolytic to Homolytic H_2 Dissociation on Nanostructured MgO(001) Films As a Function of the Metal Support, *J. Phys. Chem. C* **117**, 10623 (2013).

[177] H. V. Thang and G. Pacchioni, H_2 Adsorption on Wurtzite ZnO and on ZnO/M(111) (M=Cu, Ag and Au) Bilayer Films, *ChemNanoMat* **5**, 932 (2019).

[178] T. Ito, M. Kuramoto, M. Yoshioka, and T. Tokuda, Active sites for hydrogen adsorption on magnesium oxide, *J. Phys. Chem.* **87**, 4411 (1983).

[179] R. Eischens, W. Pliskin, and M. Low, The infrared spectrum of hydrogen chemisorbed on zinc oxide, *J. Catal.* **1**, 180 (1962).

[180] F. Boccuzzi, E. Borello, A. Zecchina, A. Bossi, and M. Camia, Infrared study of ZnO surface properties: I. Hydrogen and deuterium chemisorption at room temperature, *J. Catal.* **51**, 150 (1978).

[181] J. Kondo, Y. Sakata, K. Domen, K.-i. Maruya, and T. Onishi, Infrared study of hydrogen adsorbed on ZrO_2, *J. Chem. Soc., Faraday Trans.* **86**, 397 (1990).

[182] D. Fernández-Torre, J. Carrasco, M. V. Ganduglia-Pirovano, and R. Pérez, Hydrogen activation, diffusion, and clustering on CeO_2(111): A DFT+U study, *J. Chem. Phys.* **141**, 014703 (2014).

[183] M. García-Melchor and N. López, Homolytic Products from Heterolytic Paths in H_2 Dissociation on Metal Oxides: The Example of CeO_2, *J. Phys. Chem. C* **118**, 10921 (2014).

[184] F. Finocchi, J. Goniakowski, and C. Noguera, Interaction between oxygen vacancies on MgO(100), *Phys. Rev. B* **59**, 5178 (1999).

[185] K. Honkala, A. Hellman, I. N. Remediakis, A. Logadottir, A. Carlsson, S. Dahl, C. H. Christensen, and J. K. Nørskov, Ammonia Synthesis from First-Principles Calculations, *Science* **307**, 555 (2005).

[186] J. K. Nørskov, F. Abild-Pedersen, F. Studt, and T. Bligaard, Density functional theory in surface chemistry and catalysis, *Proc. Natl. Acad. Sci.* **108**, 937 (2011).

[187] M. Jørgensen and H. Grönbeck, Scaling Relations and Kinetic Monte Carlo Simulations To Bridge the Materials Gap in Heterogeneous Catalysis, *ACS Catal.* **7**, 5054 (2017).

[188] F. Calle-Vallejo, J. I. Martínez, J. M. García-Lastra, P. Sautet, and D. Loffreda, Fast Prediction of Adsorption Properties for Platinum Nanocatalysts with Generalized Coordination Numbers, *Angew. Chem. Int. Ed.* **53**, 8316 (2014).

[189] F. Calle-Vallejo, J. Tymoczko, V. Colic, Q. H. Vu, M. D. Pohl, K. Morgenstern, D. Loffreda, P. Sautet, W. Schuhmann, and A. S. Bandarenka, Finding optimal surface sites on heterogeneous catalysts by counting nearest neighbors, *Science* **350**, 185 (2015).

[190] M. T. Darby, M. Stamatakis, A. Michaelides, and E. C. H. Sykes, Lonely Atoms with Special Gifts: Breaking Linear Scaling Relationships in Heterogeneous Catalysis with Single-Atom Alloys, *J. Phys. Chem. Lett.* **9**, 5636 (2018).

[191] G. Kyriakou, M. B. Boucher, A. D. Jewell, E. A. Lewis, T. J. Lawton, A. E. Baber, H. L. Tierney, M. Flytzani-Stephanopoulos, and E. C. H. Sykes, Isolated Metal Atom Geometries as a Strategy for Selective Heterogeneous Hydrogenations, *Science* **335**, 1209 (2012).

[192] H. Thirumalai and J. R. Kitchin, Investigating the Reactivity of Single Atom Alloys Using Density Functional Theory, *Top. Catal.* **61**, 462 (2018).

[193] M. B. Boucher, B. Zugic, G. Cladaras, J. Kammert, M. D. Marcinkowski, T. J. Lawton, E. C. H. Sykes, and M. Flytzani-Stephanopoulos, Single atom alloy surface analogs in $Pd_{0.18}Cu_{15}$ nanoparticles for selective hydrogenation reactions, *Phys. Chem. Chem. Phys.* **15**, 12187 (2013).

[194] P. Aich, H. Wei, B. Basan, A. J. Kropf, N. M. Schweitzer, C. L. Marshall, J. T. Miller, and R. Meyer, Single-Atom Alloy Pd–Ag Catalyst for Selective Hydrogenation of Acrolein, *J. Phys. Chem. C* **119**, 18140 (2015).

[195] J. Liu, J. Shan, F. R. Lucci, S. Cao, E. C. H. Sykes, and M. Flytzani-Stephanopoulos, Palladium-gold single atom alloy catalysts for liquid phase selective hydrogenation of 1-hexyne, *Catal. Sci. Technol.* **7**, 4276 (2017).

[196] M. T. Darby, E. C. H. Sykes, A. Michaelides, and M. Stamatakis, Carbon Monoxide Poisoning Resistance and Structural Stability of Single Atom Alloys, *Top. Catal.* **61**, 428 (2018).

[197] K. G. Papanikolaou, M. T. Darby, and M. Stamatakis, CO-Induced Aggregation and Segregation of Highly Dilute Alloys: A Density Functional Theory Study, *J. Phys. Chem. C* **123**, 9128 (2019).

[198] F. R. Lucci, M. T. Darby, M. F. G. Mattera, C. J. Ivimey, A. J. Therrien, A. Michaelides, M. Stamatakis, and E. C. H. Sykes, Controlling Hydrogen Acti-

vation, Spillover, and Desorption with Pd–Au Single-Atom Alloys, *J. Phys. Chem. Lett.* **7**, 480 (2016).

[199] A. E. Baber, H. L. Tierney, and E. C. H. Sykes, Atomic-Scale Geometry and Electronic Structure of Catalytically Important Pd/Au Alloys, *ACS Nano* **4**, 1637 (2010).

[200] W. E. Kaden, T. Wu, W. A. Kunkel, and S. L. Anderson, Electronic Structure Controls Reactivity of Size-Selected Pd Clusters Adsorbed on TiO_2 Surfaces, *Science* **326**, 826 (2009).

[201] S. Abbet, A. Sanchez, U. Heiz, W.-D. Schneider, A. M. Ferrari, G. Pacchioni, and N. Rösch, Acetylene Cyclotrimerization on Supported Size-Selected Pd_n Clusters ($1 \leq n \leq 30$): One Atom Is Enough!, *J. Am. Chem. Soc.* **122**, 3453 (2000).

[202] S. Gautier, S. N. Steinmann, C. Michel, P. Fleurat-Lessard, and P. Sautet, Molecular adsorption at Pt(111). How accurate are DFT functionals?, *Phys. Chem. Chem. Phys.* **17**, 28921 (2015).